DOT/FAA/TC-14/27

Federal Aviation Administration
William J. Hughes Technical Center
Aviation Research Division
Atlantic City International Airport
New Jersey 08405

Nondestructive Evaluation for Damage in Composites and Their Repair

January 2015

Final Report

This document is available to the U.S. public through the National Technical Information Services (NTIS), Springfield, Virginia 22161.

This document is also available from the Federal Aviation Administration William J. Hughes Technical Center at actlibrary.tc.faa.gov.

U.S. Department of Transportation
Federal Aviation Administration

NOTICE

This document is disseminated under the sponsorship of the U.S. Department of Transportation in the interest of information exchange. The U.S. Government assumes no liability for the contents or use thereof. The U.S. Government does not endorse products or manufacturers. Trade or manufacturers' names appear herein solely because they are considered essential to the objective of this report. The findings and conclusions in this report are those of the author(s) and do not necessarily represent the views of the funding agency. This document does not constitute FAA policy. Consult the FAA sponsoring organization listed on the Technical Documentation page as to its use.

This report is available at the Federal Aviation Administration William J. Hughes Technical Center's Full-Text Technical Reports page: actlibrary.tc.faa.gov in Adobe Acrobat portable document format (PDF).

Technical Report Documentation Page

1. Report No.	2. Government Accession No.	3. Recipient's Catalog No.
DOT/FAA/TC-14/27		

4. Title and Subtitle	5. Report Date
NONDESTRUCTIVE EVALUATION FOR DAMAGE IN COMPOSITES AND THEIR REPAIR	January 2015
	6. Performing Organization Code
7. Author(s)	8. Performing Organization Report No.
Dan Barnard	
9. Performing Organization Name and Address	10. Work Unit No. (TRAIS)
Iowa State University 1915 Scholl Road Ames, Iowa 50011	
	11. Contract or Grant No.
	10-G-002
12. Sponsoring Agency Name and Address	13. Type of Report and Period Covered
U.S. Department of Transportation Federal Aviation Administration 950 L'Enfant Plaza FAA National Headquarters 950 L'Enfant Plaza North, SW Washington, DC 20024	Final Report
	14. Sponsoring Agency Code
	AFS-300

15. Supplementary Notes

The Federal Aviation Administration William J. Hughes Technical Center Aviation Research Division Technical Monitor was David Westlund.

16. Abstract

Several nondestructive modalities were evaluated for sensitivity to impact damage in composite structures, including mechanical hysteresis, through-transmission and one-sided pitch/catch (OSPC) ultrasonic testing (UT), and instrumented tap test on both solid laminates and honeycomb sandwich specimens. Mechanical hysteresis measurements showed that a lightweight tap mass (and subsequent low-energy tap impacts) could not deflect the part surface sufficiently to cause a strong nonlinear response from the structure. Although a heavier mass tapper could impart enough energy to cause a significant nonlinear response, increased damage due to the higher energy impacts could also occur. With a lightweight tap mass, hysteretic (nonlinear) response was low, with an overall sensitivity comparable to an instrumented tap test measure of contact time (τ) or stiffness (K). Air coupled UT measurements, particularly OSPC methods, show significant utility for identifying damage in both solid laminates and sandwich structures as well as anomalous manufacturing defects, such as marcels (out-of-plane fiber waves) and resin-starved (i.e., dry patch) areas.

17. Key Words	18. Distribution Statement
Nondestructive, Composite, Honeycomb, Tap test, Ultrasonic, Impact damage, Mechanical hysteresis	This document is available to the U.S. public through the National Technical Information Service (NTIS), Springfield, Virginia 22161. This document is also available from the Federal Aviation Administration William J. Hughes Technical Center at actlibrary.tc.faa.gov.

19. Security Classif. (of this report)	20. Security Classif. (of this page)	21. No. of Pages	22. Price
Unclassified	Unclassified	68	

Form DOT F 1700.7 (8-72) Reproduction of completed page authorized

ACKNOWLEDGMENT

This work was supported by the Federal Aviation Administration under Contract #DTFACT-09-C-00004 and performed at Iowa State University's Center for Nondestructive Evaluation (CNDE) as part of the Center for Aviation Systems Reliability Program. The technical monitors were David Galella and Paul Swindell. We greatly acknowledge the cooperation and assistance of Jay Amos of Cessna Aircraft, Jeff Kollgaard and David Messner of Boeing Aircraft, Robert Stevens of United Airlines, and Alex Melton of Delta Airlines for answers to questions regarding composites in general and honeycomb composite repairs in particular. We would specifically like to thank Alex Melton of Delta Airlines for the generous gift of two Airbus rudders, parts of which were used in this study and the remainder of which will be used for study for years to come, both in sponsored research and laboratory classes in the Iowa State University engineering curricula.

Finally, we would like to thank our students—Tom Rohlfing, Andrew Patz, Lucy Freneau-Smart, Alex Fagen, Dan Forsman, and Zi Rui Pua—for their excellent assistance in the laboratory and tireless efforts related to programming/software development. We would also like to thank visiting scientist Dr. Imran Oral of Selcuk University, Konya, Turkey, for assisting in air-coupled ultrasonic testing, computer-aided tap tester and instrumented pendulum measurements, and data analysis. Apart from those listed above, who contributed to this project, one of the authors would like to thank, in particular, the other author, Dr. David Hsu, for his hard work, innovation, and continuous example. Dr. Hsu's cheerful nature and simple but robust approach to experimentation, research, and life have been an example to all the staff and students at CNDE.

TABLE OF CONTENTS

			Page
EXECUTIVE SUMMARY			xii
1.	INTRODUCTION		1
	1.1	Objective	1
	1.2	Background	1
		1.2.1 Composite Damage Assessment Using Mechanical Hysteresis	3
	1.3	Technical Approach	5
2.	AIRCRAFT COMPOSITE SANDWICH STRUCTURES		6
	2.1	The H/C Sandwich Structures—Construction	6
	2.2	Damage in H/C Sandwich Structures	7
3.	MECHANICAL HYSTERESIS		8
	3.1	Quasi-Static Method	8
	3.2	Dynamic Method	8
	3.3	Equipment Development	9
		3.3.1 Electronics Hardware	9
		3.3.2 Motorized Tapper Design	11
		3.3.3 Software	13
	3.4	Experimental Testing—H/C Composites	16
		3.4.1 The H/C Samples	16
		3.4.2 Pre-Impact Survey	16
		3.4.3 Damage via Impact	19
		3.4.4 Post-Impact Inspection—CATT	19
		3.4.5 Post-Impact Inspection—ACUT	20
		3.4.6 Post-Impact Inspection—Sine Reference Method	22
	3.5	Results and Analysis	23
		3.5.1 Additional Post-Impact Inspection—Pendulum Tapping	24
4.	EXPLORATION OF NDI FOR SOLID LAMINATES		29
	4.1	Motivation	29
	4.2	Background of NDI for Solid Laminates	30

4.2.1 Tap Test Using Heavier Mass 30
4.2.2 Exploration of Composite NDI Using Acoustic Spectrum of Tap Test 32
4.2.3 The NDI of Solid Laminates 32
4.2.4 One-Sided Pitch-Catch Air-Coupled Ultrasound 42

5. CONCLUSIONS 43

5.1 Future Directions 44

6. REFERENCES 45

APPENDIX

A—Publications and Presentations, Book Chapter, List of Field Tests/Demonstrations, List of Collaborators, Examples of Software Code

LIST OF FIGURES

Figure		Page
1	In-Flight Detachment of Composite Rudder on Air Transat A310-300 in March 2005	2
2	Inspecting Helicopter Rotor Blade Damage With Air-Coupled Transmission Ultrasonic C-Scan	3
3	A Hysteresis Loop Decreases in Slope and Increases in Enclosed Area as the Impact Energy Increases	4
4	Integrating Acceleration Curve of Tap Test Twice to Obtain Displacement Curve	4
5	Agreement Between Dynamic Hysteresis Loop Deduced From Tap Test and Static Hysteresis Loop Obtained From Compressive Load Test	5
6	Various Types of H/C Sandwich Structures Found on Aircraft	7
7	Morphology of Impact Damage: Caternary-Shaped Fracture and One Half of the Fracture in a Fiberglass Core Sample	8
8	The 100kHz A/D Tap and Loop Data With 380kHz A/D Data Capture Example	10
9	Electronics Hardware: PCB and Main Electronic Components	11
10	Partially Assembled Motorized Tapper and Complete Motorized Tapper	12
11	Oscilloscope Traces of Hand Tap and Motorized Tapper Response Demonstrating Lower Peak Amplitude Variation and Graph Showing Minimized Tap Variation With Control of Motorized Tapper Speed	12
12	Loss of Data Without the Use of Pre-Trigger Buffer	13
13	Hysteresis Loops Over Undamaged and Damaged Area, Raw and Normalized, and Sine Reference Method Showing Raw Data, Constructed Sine Reference, and Difference Traces	15
14	Delta Sample A, ACUT Amplitude C-Scan Showing Local Variation in the Sample	17
15	Delta Samples A–E, ACUT Amplitude C-Scans Showing Local Variation in the Samples	17
16	Delta Sample A: CATT Tau C-Scan Showing Local Variation in the Sample	18
17	Delta Samples A–E: CATT Tau C-Scans Showing Local Variation in the Sample, but No Prior Damage and Uniform Central Regions for Impact Tests	18
18	Sample A—Post-Impact CATT C-Scan Showing Damage Areas	19

19	Mosaic of Samples A–E, From CATT Scan Images, Showing Internal Structure and Impact Damage	20
20	A 120 kHz ACUT C-Scan of Impact Damage Region on Sample Superimposed on Full Scan	21
21	Mosaic of 120 kHz ACUT Scans Over Damage Region on Samples A–E Superimposed on Full Scans	21
22	Unprocessed SRDA Scan and Threshold Image Delineating Flaw Region	22
23	Threshold Images for All Impact Sites, All Samples	23
24	Equivalent Flaw Size as Determined From the Noted Inspection Modalities for Various Impact Energies	24
25	Pendulum Tapping Fixture Used for Collection of Very Stable Tap Data	25
26	Hysteresis Loop Area and Normalized Hysteresis Loop Area vs. Position With Respect to Flaw Center	26
27	Normalized Tau vs. Position With Respect to Flaw Center	27
28	Normalized SRDA vs. Position With Respect to Flaw Center	27
29	Normalized Damping Coefficient vs. Position With Respect to Flaw Center	28
30	Normalized Peak Acceleration vs. Position With Respect to Flaw Center	28
31	Contact Time as a Function of Tapping Mass for Composite Solid Laminates	31
32	Acoustic Spectra of Tapping a Random Skin With a Half-Ounce Mass Over a Disbond and an Intact Region and Acoustic Spectra of Tapping a 1/2-Inch-Thick Solid Laminate of Glass Composite on and off a Saw Cut at Its Mid-Plane	32
33	Schematic Diagram of Impact Damage on the Cross Section Plane and Ultrasonic Image of the Delaminations Caused by Impact	33
34	Instron Dynatup 8200 Impact Tester and Impact Damages Made on a 24-Ply Woven GFRP Solid Laminate at Different Impact Energies	34
35	Time of Flight Immersion C-Scan Image of Impact Damage With Almost No Delamination and One With Extensive Delamination	35
36	Spatial Distribution of Microcrack Density Produced by Impact Energies of 9, 10, and 11 Joules	36
37	Microcracks in Woven GFRP Produced by an Impact With 10 Joules of Incident Energy	36

38 A Small Region of the Cross Section of Impacted GFRP Laminate Before and After Fatigue Test 37

39 Delaminations With Large COD Produced by High Impact Energy of 16 J, Block the Ultrasonic Beam Efficiently and Delaminations With Small COD and Short Length Grown From Microcracks During Fatigue Test Were Not Easily Detectable With Ultrasound 38

40 A Matrix Crack in a 90-Degree Ply Widened During Fatigue Test and Initiated Delaminations in Both Directions, and the Propagation of a Wide Delamination in a Resin Layer Between a 0-Degree Ply and 90-Degree Ply 40

41 Changes of Microcracks During Fatigue of a Region to the Right of an 18.5-Joule Impact in a 24-Ply 6S Laminate of Carbon Composite Before Fatigue and After Fatigue 40

42 Morphology of an Impact-Damaged 24-Ply 6S Laminate of Carbon Composite After Failure in Fatigue Test 41

43 The Impact Damage and Fatigue Failure Process 41

44 One-Sided, Pitch-Catch Air UT Setup and Signal Produced by Impact Damage in GFRP Laminate and Foam Block Transducer Holder Used on Wind Turbine Blade Trailing Edge 43

LIST OF TABLES

Table		Page
1	Example Comparison of Hysteretic Characterization Methods	15
2	Impact Samples—Delta Air Lines Airbus Rudder	16

LIST OF ACRONYMS

ACUT	Air-coupled ultrasonic transmission
A/D	Analog-to-digital
BVID	Barely visible impact damage
CATT	Computer-aided tap tester
CNDE	Center for Nondestructive Evaluation
COD	Crack opening displacement
FBH	Flat-bottom hole
FAA	Federal Aviation Administration
GenScan	Generic Scanner
GFRP	Glass fiber reinforced plastic
H/C	Honeycomb
NDE	Nondestructive evaluation
NDI	Nondestructive inspection
NDT	Nondestructive testing
PCB	Printed Circuit Board
OSPC	One-sided pitch/catch
SRDA	Sine reference difference area
UT	Ultrasonic testing

EXECUTIVE SUMMARY

As part of this project, a portable measurement system was designed, fabricated, and tested to evaluate the sensitivity of mechanical hysteresis or other nonlinear measurements for characterizing damage caused by impacts in honeycomb composite sandwich structures. The measurement system employed an accelerometer as both the primary tapping mass and instrument, with acceleration data captured during the contact period between the tapping mass and the specimen under test. The system design employs digital electronics to condition and measure the acceleration signal, control a motorized gear train to lift and accelerate the tap mass, and process acceleration data, then send it to a computer employing software to map the accelerometer response with respect to local position on the test specimen. The standard method of determining the parameter of interest (namely hysteresis loop area) was found to be too processor-intensive for the portable system; therefore, an analog to the hysteresis measurements was developed for which the raw acceleration signal (with linear and nonlinear components) is compared to a reference half-cycle sine wave (a perfectly linear response). Test results indicate that the light mass of the accelerometer limits nonlinear behavior in both full hysteresis loop and sine reference measurements. Increasing the tap mass is not a reasonable option because damage from the increased tap force could occur.

Additional work was carried out involving examinations of damage in solid laminates by use of the tap test and audio spectrum analysis as well as ultrasonic inspection methods. Nondestructive and destructive (microscopy) testing on both glass and carbon fiber solid laminates revealed that impact energies above a particular level produced delaminations, whereas impacts below this delamination threshold produced cone-shaped arrays of microcracks.

Fatigue tests on samples impacted with energies below the identified threshold demonstrated that, with cyclic loading, the microcrack arrays coalesce into larger delaminations and finally lead to sample failure. Additional collaborative work identified several promising applications of air-coupled ultrasonic methods to solid laminates for the detection of fiber marcels, dry patches, and porosity, but in a one-sided pitch/catch (OSPC) arrangement that will significantly increase the utility of air coupled methods.

1. INTRODUCTION.

1.1 OBJECTIVE.

The objective of this project was to evaluate nondestructive evaluation (NDE) modalities for characterizing damage in composite structures and also to develop new NDE methods for the characterization task of inspectors. Of primary interest was the characterization of impact damage in honeycomb (H/C) sandwich structures through the application of mechanical hysteresis analysis. The objective of the mechanical hysteresis work was to evaluate the capability of dynamic mechanical hysteresis measurements to characterize and differentiate the degree or type of damage present in an impact on an H/C sandwich. The overall goal is always to relate an inspection modality metric with a damage metric, such as probe peak amplitude to impact energy. In addition, the inspection modality should ideally identify the type of damage present, such as crushed core, skin-to-core disband, or sandwich skin ply delamination in H/C sandwiches, which guides repair decisions. Any inspection method should ideally have the reproducibility and sensitivity to detect below-repair-threshold damage, allowing the damage to be tracked or monitored while still suitable for service, thus maximizing component utilization and minimizing costs. A continuing goal is to add imaging capability to modalities (both existing and newly developed) so that the condition and state of damage in the component and the quality of any repairs are visually presented to the inspector for evaluation and disposition.

1.2 BACKGROUND.

Composite H/C structures have been in use for many years as secondary structure and flight controls and have a reasonably good safety record, although a few major accidents have been attributed to failures in these sandwich structures. The loss of an F-15E in 2002 was attributed to the structural failure of an aluminum H/C sandwich leading edge on a vertical stabilizer. In March 2005, the rudder of a Canadian Air Transat A310-300 separated in flight over the Florida Keys (see figure 1), but the pilots managed to return and land in Havana [1]. Later in the same year, the rudder on a FedEx A300-600 was found to have large disbond between its inner skin and the H/C core. The Federal Aviation Administration (FAA) issued an airworthiness directive ordering the operators to examine the rudders of the A300 series. These incidents have also prompted Airbus and the European regulators to depart, for the first time, from their established visual-only inspection requirement for the composite rudder; instead, they've begun to require advanced nondestructive inspections (NDIs) for more than 400 A300 and A310 rudders, and approximately 20 A330 and A340 rudders in service [2].

Figure 1. In-Flight Detachment of Composite Rudder on Air Transat A310-300 in March 2005

The main rotor blades of the UH-60 Black Hawk helicopter are another example of composite H/C sandwich structure. Figure 2 shows the damage to a rotor blade sustained from a tree strike during night training, for which damage was mapped out by Iowa State University's Center for Nondestructive Evaluation (CNDE) composites group at an Air National Guard base using an air-coupled ultrasonic transmission (ACUT) C-scan [3] and the computer-aided tap tester (CATT) system. Composite sandwich structures on an aircraft may suffer from various types of damage while in service (ranging from mechanical impact resulting from hail to bird strike, foreign object damage, and tool-drop), causing delamination in the facesheet, disbond of the facesheet from the core, and crushed H/C core. Water ingression or hydraulic fluid leakage can degrade the adhesive bond and lead to separation of the skin and core. Such damage conditions must be detected at an early stage so that the structure may be repaired and major structural failures can be avoided. After the structures are repaired, the quality of the repair and its continued airworthiness should be verified with NDI techniques. The NDI techniques used by the inspectors for detecting and evaluating defects and damage on composite sandwich structures are mostly qualitative. In practice, the hearing-based manual tap test is still the widely used NDI technique for composite sandwich structures. Conventional contact mode ultrasonic inspection is of very limited use on H/C sandwiches. Air-coupled through-transmission ultrasonic inspection, although effective, requires more elaborate equipment. Other, more sophisticated nondestructive testing (NDT) methods requiring expensive instrumentation include thermography and shearography.

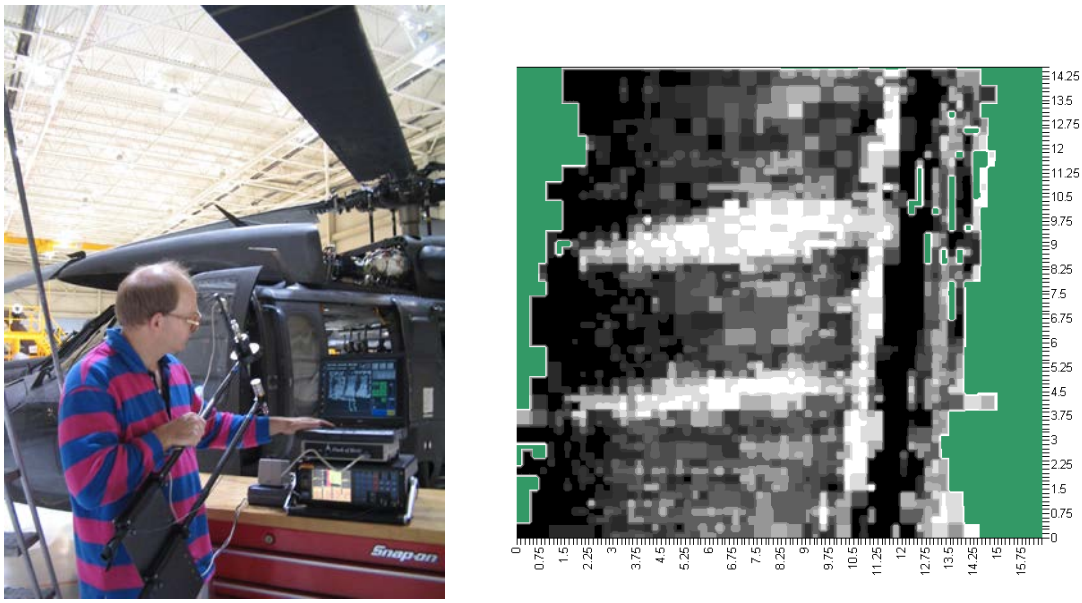

Figure 2. Inspecting Helicopter Rotor Blade Damage With Air-Coupled Transmission Ultrasonic C-Scan (The two horizontal white bands are crushed core damage caused by a tree strike.)

With previous FAA funding, the CNDE composites group developed an instrumented tap test system—the CATT—that provides an image of the size and shape of the defect and damage [4 and 5]. In addition, the CATT uses an accelerometer with a hard steel tup as the tapping mass. Because the steel tup is so much stiffer than composite sandwich panels, the local out-of-plane stiffness, and the stiffness degradation in the H/C sandwich due to damage, can be deduced from the time of contact (τ) between the tup and the part surface, which was measured by the electronic circuit of the CATT device [6]. Although the CATT has imaging capability and has made the tap test significantly more quantitative than a standard hearing-based tap test, the contact time (τ) is a parameter that falls short in efforts to quantitatively evaluate the degree of damage on composite sandwich structures. The desire for a more sensitive metric to measure the damage present in H/C composite structures motivated the current work.

1.2.1 Composite Damage Assessment Using Mechanical Hysteresis.

In the study of composite damage behavior conducted at Iowa State in recent years, it was recognized that the energy-dissipative nature of the internal damages in composite structures can lead to nonlinearity and hysteresis in their mechanical response [7 and 8]. The load and unload curves in a compression test conducted on a laboratory mechanical testing machine combined to form a hysteresis loop. As the damage became more severe, the enclosed area of the loop increased and the slope of the loop decreased, as shown in figure 3. However, to exploit the hysteresis data as a means of evaluating the damage severity in the field, a one-sided test method was needed. It was further discovered that a dynamic hysteresis loop may be deduced from the acceleration-versus-time data of a tap test. With an accelerometer attached to the tapping mass, the voltage output of the accelerometer can be converted into acceleration based on the sensitivity (such as 10 mV/g). The displacement-versus-time curve can be obtained by

integrating the acceleration curve twice, as shown in figure 4. Since the tapping mass is known, the force ($F = ma$) is calculated and a dynamic load-displacement loop is then constructed. On H/C panels containing impact damage, the static hysteresis loop obtained from the compression test and the dynamic hysteresis loop deduced from a one-sided tap test were found to agree in shape and slope after normalization, as shown in figure 5. Compared to the local tensile test of the elasticity laminate checker, the hysteresis loop is an indication of the energy dissipation associated with the meshing of the fractured or buckled cell walls under a compressive load. It is believed to be a better indicator for the severity of damage than the drop in stiffness (K) deduced in a standard CATT test. It was therefore proposed that the hysteresis method be developed, based on a one-sided tap test, as a potential NDI tool for assessing the degree of damage in composites.

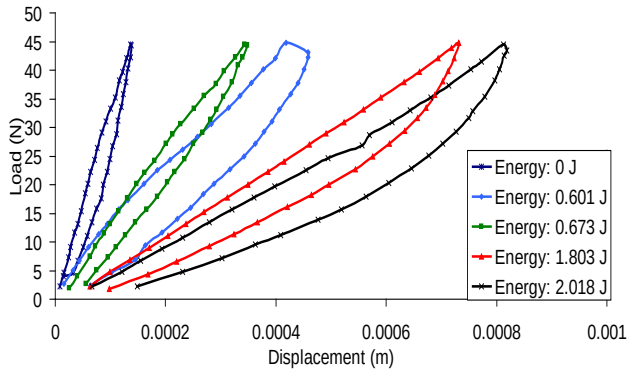

Figure 3. A Hysteresis Loop Decreases in Slope and Increases in Enclosed Area as the Impact Energy Increases

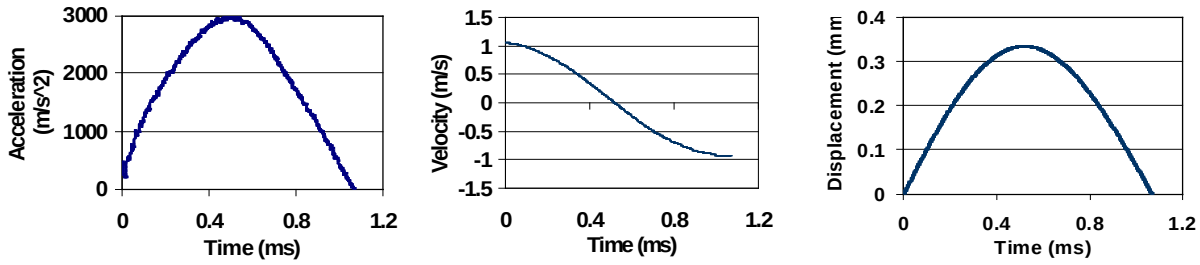

Figure 4. Integrating Acceleration Curve of Tap Test Twice to Obtain Displacement Curve

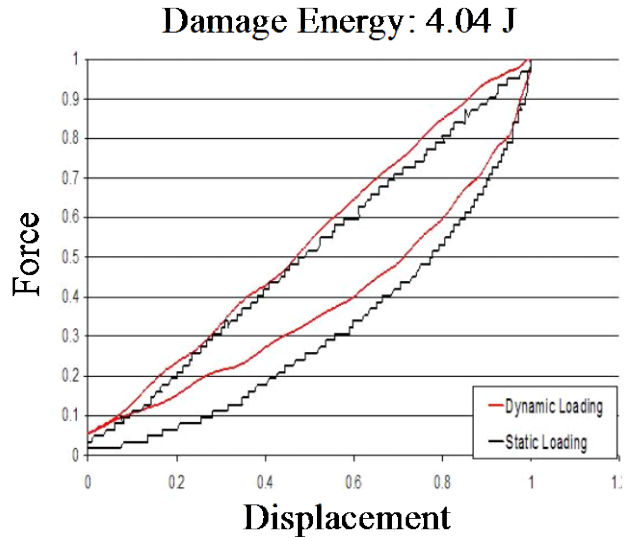

Figure 5. Agreement Between Dynamic Hysteresis Loop Deduced From Tap Test and Static Hysteresis Loop Obtained From Compressive Load Test

1.3 TECHNICAL APPROACH.

As described in section 1.2, the load-displacement behavior of a damaged composite structure becomes nonlinear and the load and unload curves in a static compression test combine to form a hysteresis loop. The area enclosed by the hysteresis loop is an indication of the severity of the internal damage. For this project, it was proposed that a hysteresis loop be deduced from the force-time history of a simple one-sided tap test using an accelerometer as the tapping mass, as used in the previously developed CATT system. When an accelerometer of a given mass and sensitivity (for example, 10 mV/g) is used as the tapping mass, the voltage output is the acceleration as a function of time. The acceleration-versus-time data of the tap can be integrated to obtain the velocity, which can in turn be integrated again to obtain the displacement. Because the mass of the accelerometer is known, the acceleration converts directly to force and a load-displacement plot can then be made. Figure 5 shows that the dynamic hysteresis curve deduced from acceleration data agrees with the static hysteresis loop, in shape and in slope, from a compression test.

The goal of this project was to develop a means for making reproducible and controlled tap tests and to develop a robust double integration procedure (or analogous method) for deducing the nonlinear (hysteretic) response of damage via an instrumented tapper. Such parameters as the enclosed loop area, loop slope, or delta-V (the difference in initial and final tap velocities) were analyzed for a quantitative correlation with the damage severity in composite structures. The damage severity can be quantified in terms of the impact energy that caused the damage. Impacts on previously undamaged composites were made using the available Instron 8200 instrumented impact tower to ensure controlled damage inputs for the developed measurement system to evaluate. Prior to and after the controlled impacts on the test specimens, other available NDI methods were used to evaluate the before/after state of the specimens, including the standard CATT and ACUT methods. The eventual goal was to develop the testing technique

to a stage at which an inspector could manually tap the surface of a damaged part and the associated software would provide an assessment of the severity of the damage.

The initial studies described in section 1.2 were conducted using an oscilloscope to digitize the output voltage of the accelerometer. For practical inspection using the hysteresis method, the data acquisition and processing electronics must be much simpler and compact. The development of the necessary hardware and software was a major effort of the project. To ensure that the tapping of the surface with an accelerometer can be done in a reproducible and controlled manner, a mechanical device (a motorized tapper) was designed, developed, and optimized.

2. AIRCRAFT COMPOSITE SANDWICH STRUCTURES.

2.1 THE H/C SANDWICH STRUCTURES—CONSTRUCTION.

A wide variety of composite sandwich panel designs using H/C as the core material are employed on aircraft as nonprimary structures or flight-control surfaces. Some example structures and components include spoilers, slats and flaps, fairings, engine cowlings, landing gear doors, and rudders. Component materials include skins of carbon, Kevlar® and glass fibers, matrix materials of epoxy, and cores of Nomex® or fiberglass H/C. Although a materials list should include metal skin/metal H/C core designs, the focus of this project was on polymer/fiber composites materials. Figure 6 displays several commonly deployed designs of H/C core sandwiches.

In H/C composite constructions, skin thickness will range from a few plies (0.020 inch/0.5mm) to several millimeters and cores from 0.25 inch (6mm) to several inches in thickness. Structure/geometrical conditions, such as curvature (simple or compound), multiple core materials with septums, perforated skins, ply drops and core density changes, and tapering thicknesses complicate construction, but these conditions can also severely limit or impede inspections.

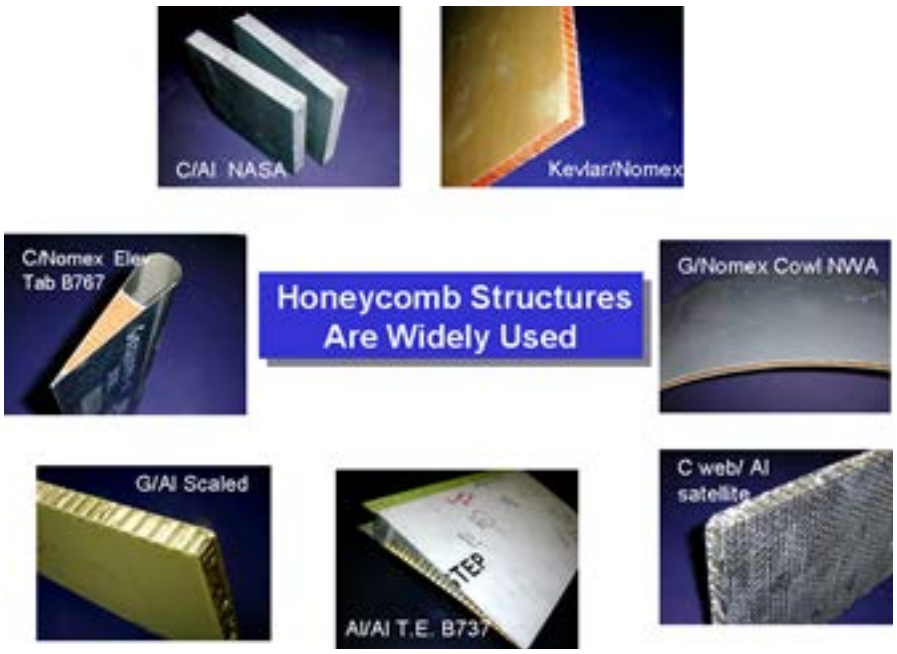

Figure 6. Various Types of H/C Sandwich Structures Found on Aircraft

2.2 DAMAGE IN H/C SANDWICH STRUCTURES.

The main concern of service-induced damage for composite H/C structures is impact damage caused by various reasons, including hail, runway debris during takeoff and landing, and tool drop and impact by ground handling equipment during maintenance. The morphology of impact damage depends on the skin and core material type, but also the energy of impact. Damage types include delaminations between plies of the skin laminate, skin to core disbonds, or crushed or fractured cores. For example, impacts above some threshold energy value on sandwich panels with Nomex or fiberglass core would cause a fracture of the H/C cells inside in the shape of a catenary, with the greatest depth under the point of impact and tapering upward toward the skin further away from the center. Figure 7 shows the shape of the fracture of the H/C cell walls and a portion of the fiberglass core in an impacted trailing edge.

A unique feature about impact damage on composite H/C panels is that low-energy impacts usually leave no visible sign on the surface but may cause disbond, delaminations, or core fracture inside. The detection of nonvisible or “barely visible” impact damages (BVID) is very important on composite structures. In a crushed/fractured core condition, because of the reduced contact stiffness on the surface, such conditions can usually be detected and imaged with instrumented tap test devices such as the CATT. The discontinuity associated with the fracture also affords itself to detection by air-coupled ultrasound in the transmission mode, as do disbonds and delaminations. With both these inspection methods, however, identifying the type of damage is typically not possible. In transmission mode (e.g., ACUT), all three of the damage types noted blocked transmission of sound through the sample, so all appear as low-amplitude regions with little or no contrast between the damage types.

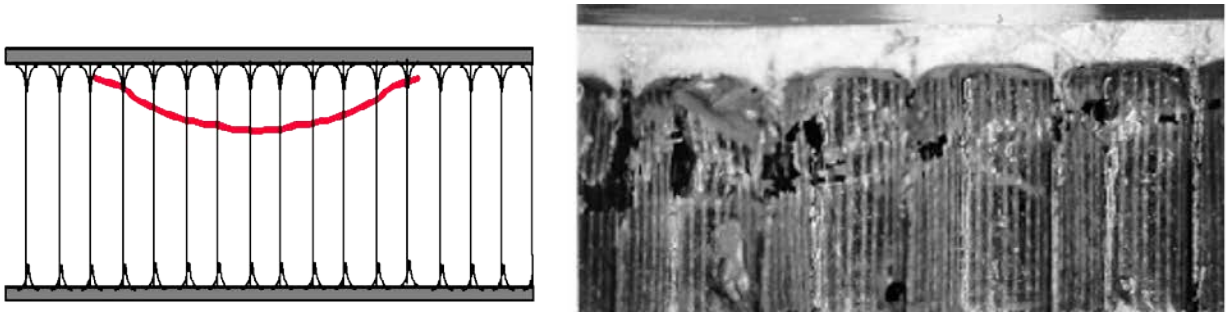

Figure 7. Morphology of Impact Damage: Caternary-Shaped Fracture (left) and One Half of the Fracture in a Fiberglass Core Sample (right)

3. MECHANICAL HYSTERESIS.

3.1 QUASI-STATIC METHOD.

As noted in section 1.2, the quasi-static method for development force displacement plots involves placing the sample under a loading apparatus that provides measures of force and displacement throughout the test. Peak loads in early work ranged from 20–40 lbf (80–200N), producing displacements in the tens of millimeters. In tests at the center of damage areas, the force-displacement plot was not linear; that is, the unloading phase did not follow the loading phase, producing a loop as shown in the previous figures and identified as mechanical hysteresis. This hysteresis is a manifestation of the nonlinear behavior of the material, particularly in the damaged state. With increased damage (from impact in these cases), the hysteretic behavior increased, demonstrated by the increase in load/displacement trace loop area. Following this initial result, additional tests were undertaken using a tap mass with an affixed accelerometer. The concept was to perform a dynamic force/displacement test, and a tap test, and to determine if similar hysteric behavior was demonstrated.

3.2 DYNAMIC METHOD.

In tests to determine if dynamic force/displacement traces could be generated and whether the hysteretic response continued to be manifested, a tap mass (a hollow steel tube of approximately 200 grams) was affixed with an accelerometer of the type used in the CATT system (model 353B04, PCB Piezotronics, Inc.). The tap response was recorded on a digital storage oscilloscope and transferred to a computer for processing. With each tap, the tapper mass was elevated to a set height and dropped. The mass was guided by linear bearings to ensure vertical orientation at impact and, although the linear bearings are low friction, tap initial velocity (velocity at impact) did vary somewhat from tap to tap.

The acceleration data were collected and transferred to a computer for analysis. Generating the force displacement plots involves determining the force (by multiplying the mass of the tapper by the acceleration values) and displacement (by double integration of the acceleration values) as a function of time, then plotting force vs. displacement. As the initial tap velocity varied by small amounts from tap to tap, adjustments to the initial velocity were made for each tap data set to produce a zero velocity at peak acceleration. As noted in section 1.2, these tests demonstrated

that a dynamic load/displacement plot could be generated that mimics the results generated by a quasi-static test.

3.3 EQUIPMENT DEVELOPMENT.

The components needed for this system involved several subsystems, including: 1) a motorized tapper to include mechanical hardware and electronics to control the speed of a motorized tapper, allowing changes in speed to optimize tap response, 2) electronics for conditioning and measurement of acceleration data (a high-speed analog to digital [A/D] converter) for each tap, 3) circuitry to make use of the Mimio components used in the previously developed Generic Scanner (GenScan) system to trigger position tracking for each tap, and 4) a supervisory microprocessor to control the data measurement, storing to memory, processing (i.e., force, velocity, displacement, and loop area), Mimio triggering, and sending loop area or other data to a computer for the generation of C-scan images.

As noted, the primary method for determining tap displacement for use in load/displacement plots is by a double integration scheme. Although this method (with a bit of adjusting for variations in the initial velocity) is reasonably robust, the adjustments needed are always made after the fact, during post-processing of the data. It would be advantageous to develop a method that would not require the adjustment of each individual tap initial velocity to achieve adequate results. If a mechanism could be developed that produced uniform tap initial velocities, then these adjustments could be eliminated.

3.3.1 Electronics Hardware.

The supervisory microprocessor chosen for this system is the propeller by Parallax, Inc. This microprocessor has a novel eight-subprocessor architecture with shared buses for memory and digital IO, high speed (5MHz base clock), and assembler coding, and is available in a package that includes a USB bus, memory, and a power supply at a low cost (~$80). Early tests—shown in figures 8(a) and 8(b)—on an A/D converter capable of 120k samples/second demonstrated that rate to be too slow, capturing too few points in an average tap, and demonstrating the need for a higher sampling rate. The A/D measurement device finally deployed was an LTC1278 12-bit, 380k samples/second A/D by Linear Technologies, Inc., with captured data shown in figure 8(a). This A/D has a parallel interface that is compatible with the propeller. Additional circuitry to condition and power the accelerometer included a voltage booster and current limiting (3mA) circuit (Maxim 662 boost converter, a variable gain amplifier (Burr Brown OPA2350 operational amplifier, and a Dallas Semiconductor DS1267 digital potentiometer. These components and other minor components were used in the design of a custom-printed circuit board (PCB) to mount and shield the components in an aluminum enclosure. Also included were connectors with power/control/data cabling for running the tapper motor, a Dymo/Mimio transmitter head, and a USB-to-serial cable for connection to the computer. The cable from the enclosure to the motorized tapper used standard analog video monitor cables because they are inexpensive and readily available, but capable of shielding the high-current motor control and high-voltage Mimio transmitter (~100 volts) conductors from the sensitive accelerometer signal conductors.

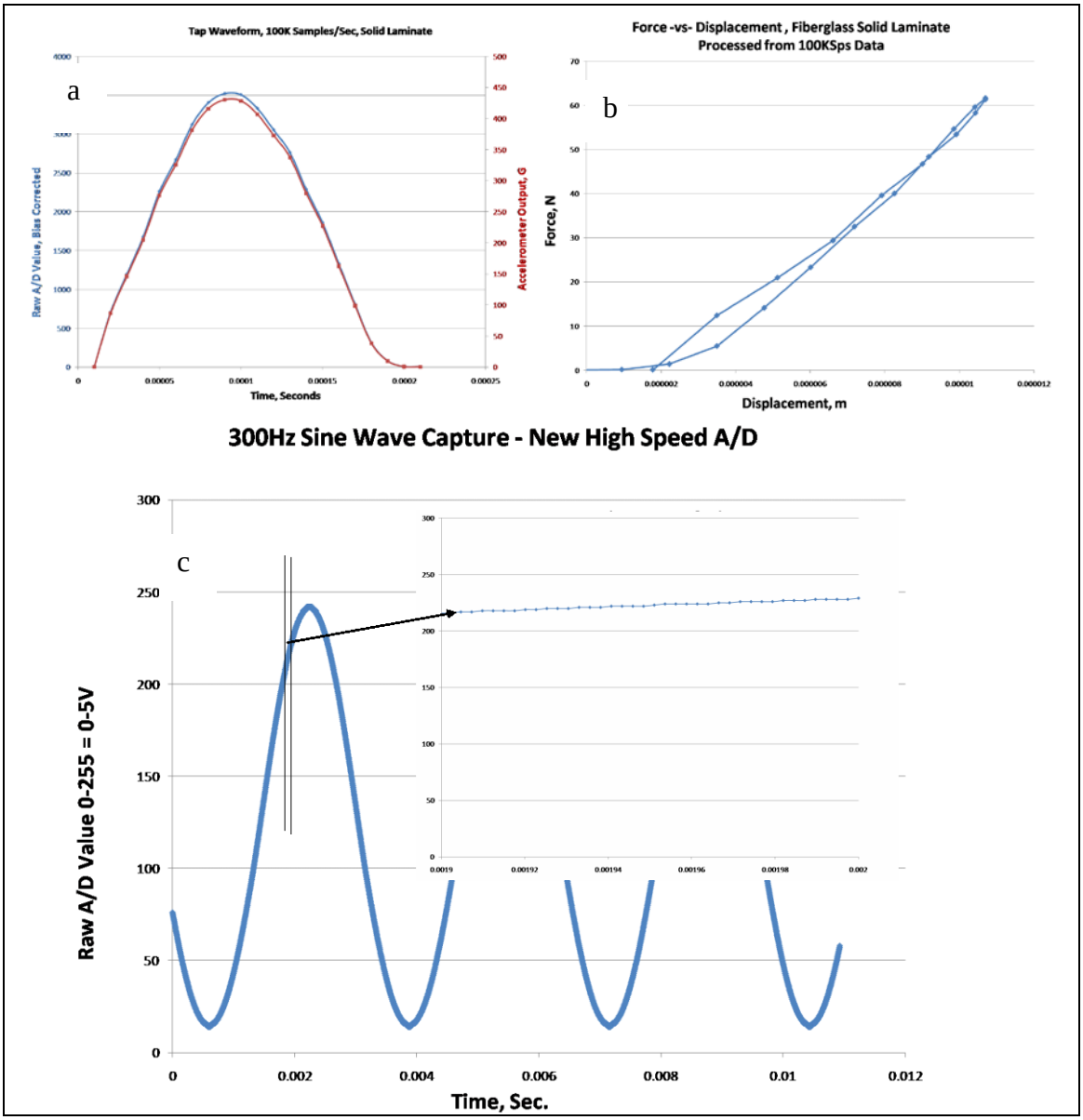

Figure 8. The (a) 100kHz A/D Tap and (b) Loop Data With (c) 380kHz A/D Data Capture Example

The motor controller chosen to power the tapper motor was a Pololu QIK 2s9v1, providing 12 volts to the motor and controlled over a serial connection to the propeller via the PCB. The Mimio transmitter electronics were removed from a Mimio stylus and modified to mount to the PCB via bus pins, with a circuit added to turn the transmitter electronics on (12ms) and off after each tap was captured by the A/D. This resulted in a nonsynchronized position tracking scheme, but with the slow scan speeds typically found in hand scanning operations (as demonstrated in the GenScan developments), position precision was typically within ±0.040″. A 12-volt NiMH rechargeable battery is included with the circuit, providing power (through a 5V regulator) to the propeller and other integrated circuits and the full 12 volts to the motor. Images of the PCB with microprocessors and associated circuit elements are shown in figure 9.

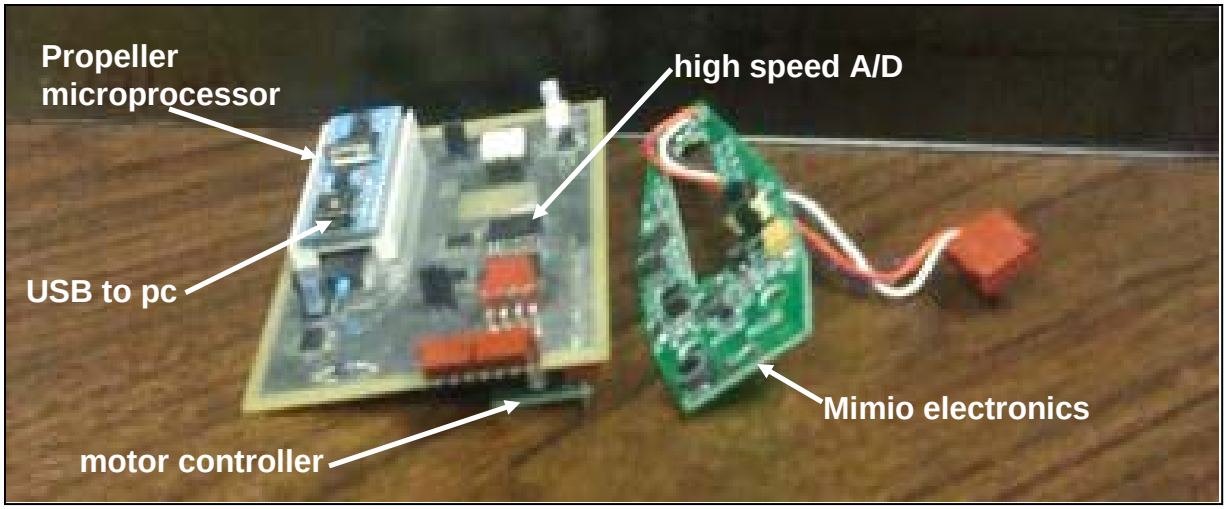

Figure 9. Electronics Hardware: PCB and Main Electronic Components

3.3.2 Motorized Tapper Design.

In previous work on a motorized tapper, a small 5-volt motor/gearbox was tested in a configuration employing a magnetic cam (magnetic wheel and yoke) similar to the CATT semi-automated cart developed under previous FAA funding. The low power 5 volt, although very inexpensive (~$12), did not have the capability to handle the intermittent torque generated by the magnet wheel/yoke, typically lasting a few hours before the plastic internal gears stripped or spun on the shafts. For this work, a more powerful 12-volt motor was chosen. This motor incorporated a 154:1 metal gear reduction with a 120-ounce-inch torque rating. A set of bevel gears and a final pair of reduction gears made up the gear train (an axis orientation change was needed to make the entire motorized tapper smaller in dimension). Pictures of a partially assembled and completed tapper unit are shown in figures 10(a) and 10(b). Note the cover for the unit, which employed a CATT semi-automated cart cover that was modified to accept the motorized tapper, connector, and Mimio transmitter head. Figure 11 depicts the oscilloscope traces, which demonstrate the consistency of taps delivered by the motorized tapper, shown here compared to hand tap results. The graph in figure 11 shows the response of the motorized tapper with respect to tap speed, for which the average Tau value stabilizes (top plateau region) and, more importantly, the standard deviation of Tau decreases at higher speeds. The highest speed control parameter (as noted on the graph x axis), a value of 128, represents a speed of approximately 35 taps/second.

Figure 10. (a) Partially Assembled Motorized Tapper and (b) Complete Motorized Tapper

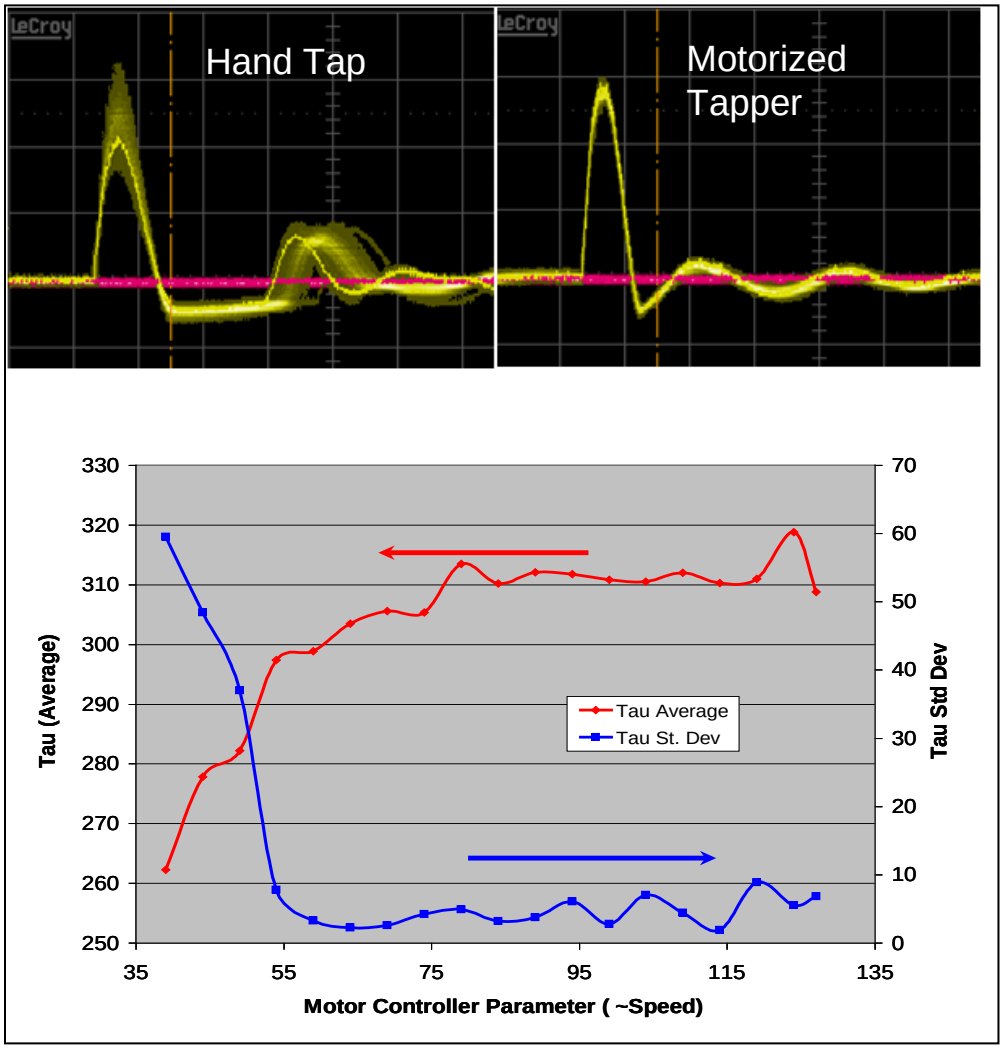

Figure 11. Oscilloscope Traces of Hand Tap and Motorized Tapper Response Demonstrating Lower Peak Amplitude Variation and Graph Showing Minimized Tap Variation (standard deviation) With Control of Motorized Tapper Speed

3.3.3 Software.

The first software codes developed controlled the high-speed A/Ds and consist of commands to continuously read the A/D value, wait for a voltage value above a particular threshold or trigger value, and then collect 500 data points. Pre-trigger values are stored in a first-in/last-out style buffer, storing 20 pre-threshold values. When each new A/D value comes in, the last value in the buffer is discarded. In this way, some pre-trigger data is retained. Figure 12 demonstrates the reason for retaining pre-trigger data; in the case of taps over a damaged area, the peak acceleration is lower and time duration of the tap longer. Without a method of retaining the pre-trigger data, a portion of the needed acceleration data is lost — and a larger portion of such data is lost in damaged areas. The 20-value deep buffer is a reasonable depth for most materials. With each trigger, 500 points (or approximately 1250μs of data) are captured; this is equivalent to a Tau typical for a heavily damaged sandwich panel.

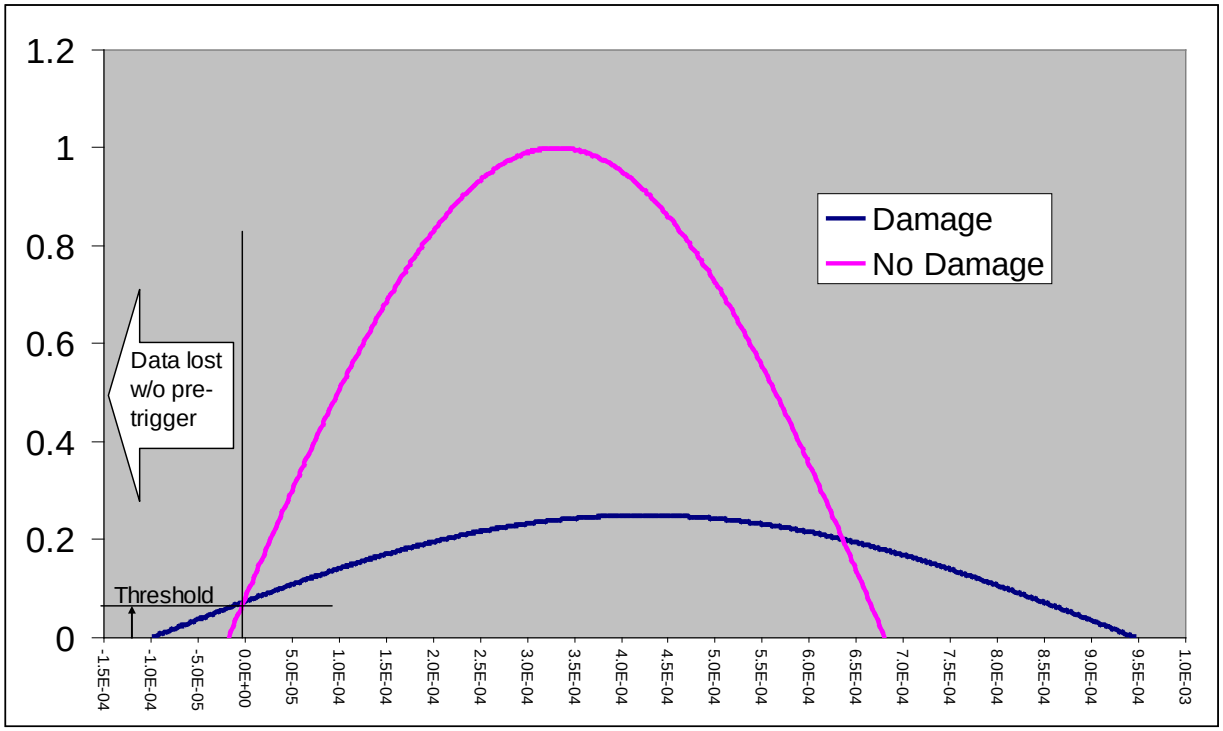

Figure 12. Loss of Data Without the Use of Pre-Trigger Buffer

The double-integration scheme for displacement determination, and the determination of a loop area from the load/displacement data, was found to be very time-consuming from a data-processing/code standpoint. These combined operations involved four or five (depending on whether normalization was needed to minimize differences in peak force) complete loops through the data set (one each for force, force normalization, velocity, and displacement loop area calculations). With a data set of 500 data points per tap, a single tap result was found to be about 37ms. This does not take into consideration other operations that would need to take place, such as sending the results out to the computer and controlling other operations, such as motor speed and Mimio triggering. This resulted in an unacceptably slow effective tap rate, even

though all of the code for control of each of the subsystems (noted above) and the supervisory code were written in an assembly language. Assembly language is the lowest level language (and, therefore, fastest) code available. Because the standard double-integration method and the loop area calculation were too slow, an alternate method to gage the nonlinear response during a tap was sought.

In considering the hysteretic response of a tap over damage, the hysteresis loop area may be thought of as a measure of distortion (i.e., a departure from linear behavior). If the behavior of the tup and material interacting is purely linear, the response is essentially a half-cycle sine wave. When material is damaged, both the load and unload phases of a tap response depart from the ideal sine wave. A test was needed to determine whether simply comparing a tap signal to an ideal half-cycle sine wave could reveal nonlinear behavior.

To test this concept, tap signals on undamaged and damaged specimens were captured and stored in a computer. For each tap, a reference sine wave was constructed using the contact time (Tau) to determine the reference sine period. The tap data amplitude was normalized to match the sine reference amplitude (peak = 1 if this normalization is similar to the quasi-static method in which each sample was loaded to the same peak load, as seen in figure 3). The raw and peak normalized loops are shown in figure 13(a) and the accelerometer signal and reference sine for the two taps, which also show the absolute difference between the tap data and reference sine, are shown in figure 13(b). The sum of the absolute difference, referred to here as the sine reference difference area (SRDA), is calculated and compared to the hysteresis loop area for the same taps. The results are shown in table 1. Prior to normalization, the loop areas for these taps are essentially equal, with the damage site exhibiting only 25% more loop area; whereas, after normalization, a significant increase in the difference is seen. Note also that the sine reference method produced a difference similar to the normalized loop area method. This difference was approximately 130%. In code, however, this method would involve only one loop through the data because it is possible to construct the sine reference, subtract the normalized accelerometer data, and sum the differences sequentially in the same loop. With these savings, it was determined that using the sine reference method instead of the double integration method to characterize hysteretic (nonlinear) behavior of damage sites would be prudent.

Other examples of software code developed involved triggering the Mimio transmitter hardware to pulse once for each tap signal measured, sending the sine reference results to a computer for use in creating C-scan images and controlling the motorized tapper. To minimize the offset in timing between the tap data collection and position determined by the Mimio electronics, rather than wait until the result of the sine reference was determined for each tap, the Mimio was triggered after each tap was measured and before the sine reference calculation began. Once the sine reference calculation loops were complete, the result was sent over a serial communications link to the PC Control of the motorized tapper. This includes motor start/stop/speed up/slow down and was made controllable through the computer software over the USB/serial link to the propeller. In addition to motor controls, system startup check options were developed for which the operator could check the operation of the tap measurement circuit and the Mimio transmitter operation via computer software. All these control features were refined from similar controls developed in the previous version of the motorized tapper.

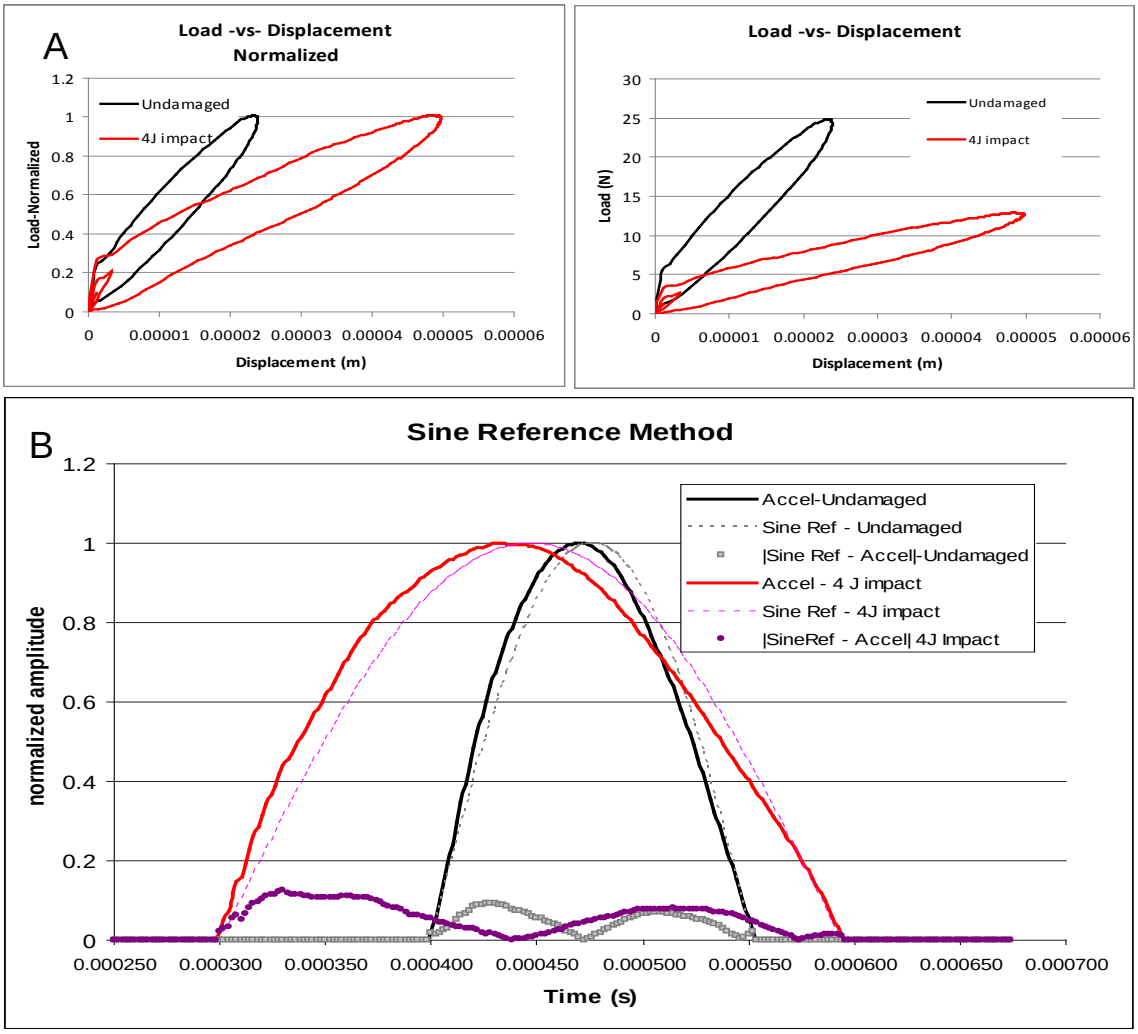

Figure 13. (a) Hysteresis Loops Over Undamaged and Damaged Area, Raw (right), and Normalized, (left) and (b) Sine Reference Method Showing Raw Data, Constructed Sine Reference, and Difference Traces

Table 1. Example Comparison of Hysteretic Characterization Methods

Sample	Raw Hysteresis Loop Area (J)	Normalized Loop Area	SRDA
Undamaged	6.30E-06	2.60	3.7
Damaged (4J impact)	7.90E-06	6.20	8.5
% Change	25%	138%	130%

Software code that controlled tapper motor speed was also developed to automatically determine the optimum tapper speed. When the operator selected this mode, the system started the motors at the highest speed, captured tap data, and calculated the standard deviation in Tau, then

lowered the speed and took another measurement. This was continued until a minimum standard deviation was found. In practice, this code did find an optimum speed for Tau measurements over undamaged areas, but it was found that this did not coincide with the optimum speed over damage areas. Eventually, this automated feature to determine speed was replaced with simple speed controls (faster/slower) that the operator could adjust until stable values were seen in the sine reference data outputs.

3.4 EXPERIMENTAL TESTING—H/C COMPOSITES.

3.4.1 The H/C Samples.

To test the developed hardware and software, an Airbus composite rudder, given to CNDE by Delta Air Lines, was disassembled and cut into smaller pieces. Each of the samples, which were of various lengths, was cut to 18″ in width to allow mounting onto the Instron 8200 instrumented impact tower. Prior to creating impact damage, the samples were surveyed with ACUT (100, 120, and 225 kHz) and the CATT system to ensure no prior damage was present. After the pre-impact survey, each sample was marked for impact sites 6″ apart across its length, excluding the closeout sections at the leading and trailing edges. Each sample was impacted at the marked locations, with the impact data recorded by the Instron instrumentation. A summary of impact data for the specimens is shown in table 2. After impact, the samples were again surveyed with ACUT, the CATT system, and the hysteresis (sine reference) measurement system.

Table 2. Impact Samples—Delta Air Lines Airbus Rudder

Sample	Impact Energy (J)	Impact Sites
Delta A	4	3
Delta B	3	4
Delta C	2	4
Delta D	1.4	4
Delta E	1	4

3.4.2 Pre-Impact Survey.

A sampling of pre-impact survey results is demonstrated in figures 14 through 17, including representative results on sample “A” and a mosaic of all samples using 120 kHz ACUT and CATT inspection methods, respectively. The images shown demonstrate that no prior damage was found in the samples, although local differences were seen that relate to differences in core density as well as core type and skin ply counts in the sample.

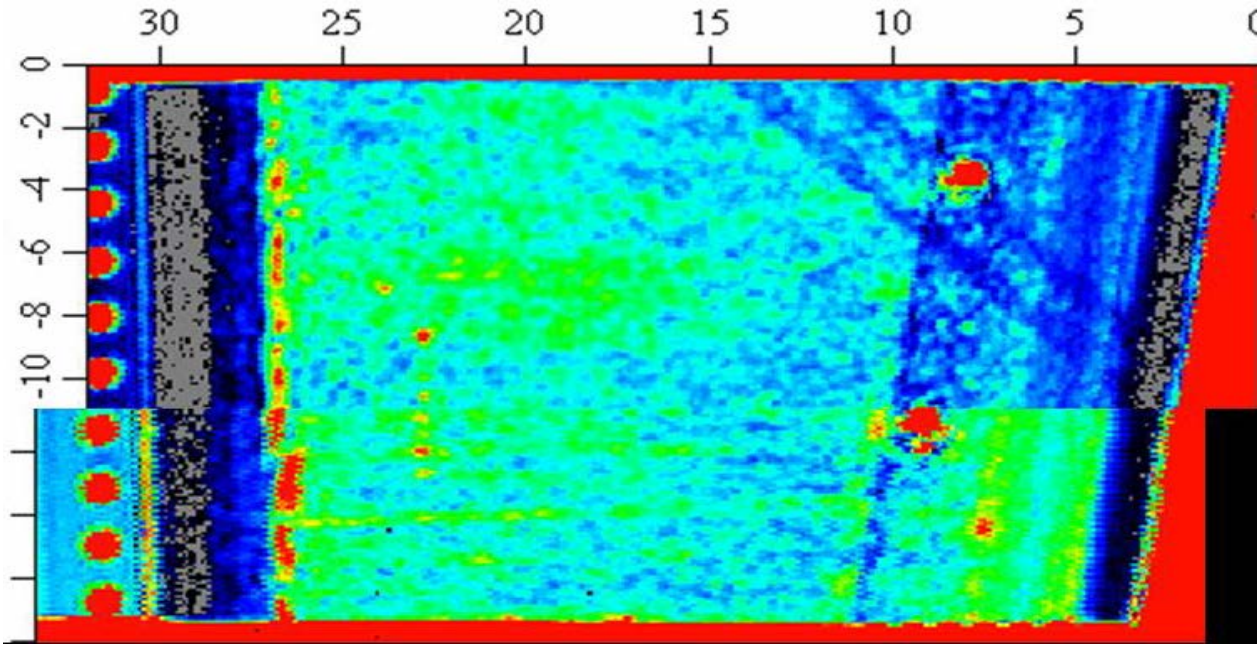

Figure 14. Delta Sample A, ACUT Amplitude C-Scan Showing Local Variation in the Sample (with nominally uniform region, between 10 and 25 inches in the scan, available for impact tests)

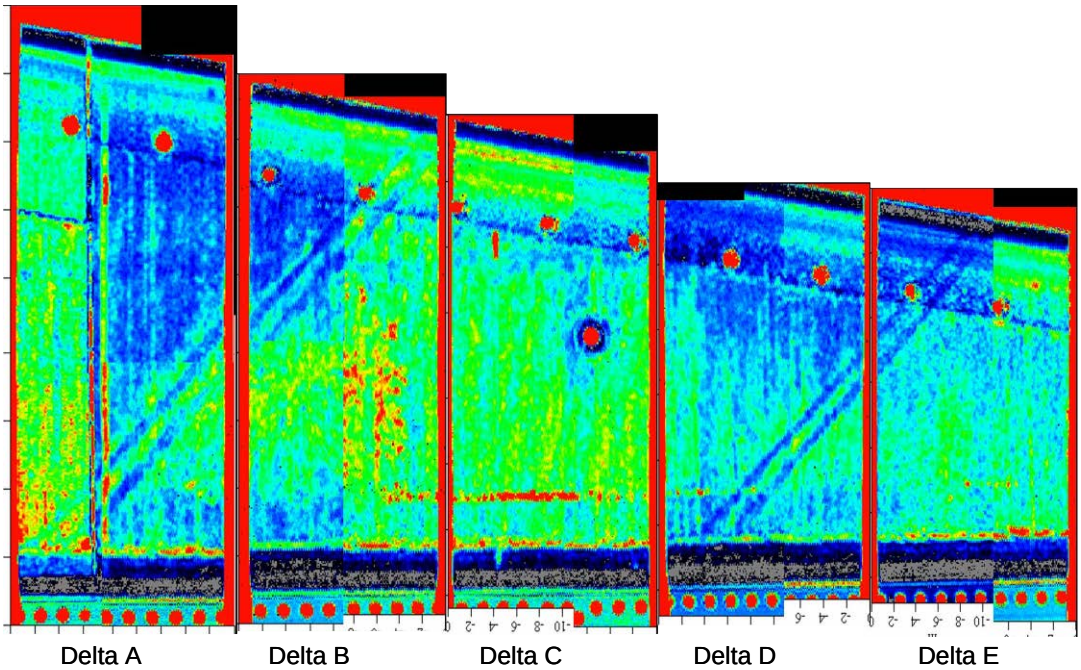

Figure 15. Delta Samples A–E, ACUT Amplitude C-Scans Showing Local Variation in the Samples (the larger red circular regions are fastener holes in the part and diagonal striping represent ply overlay areas)

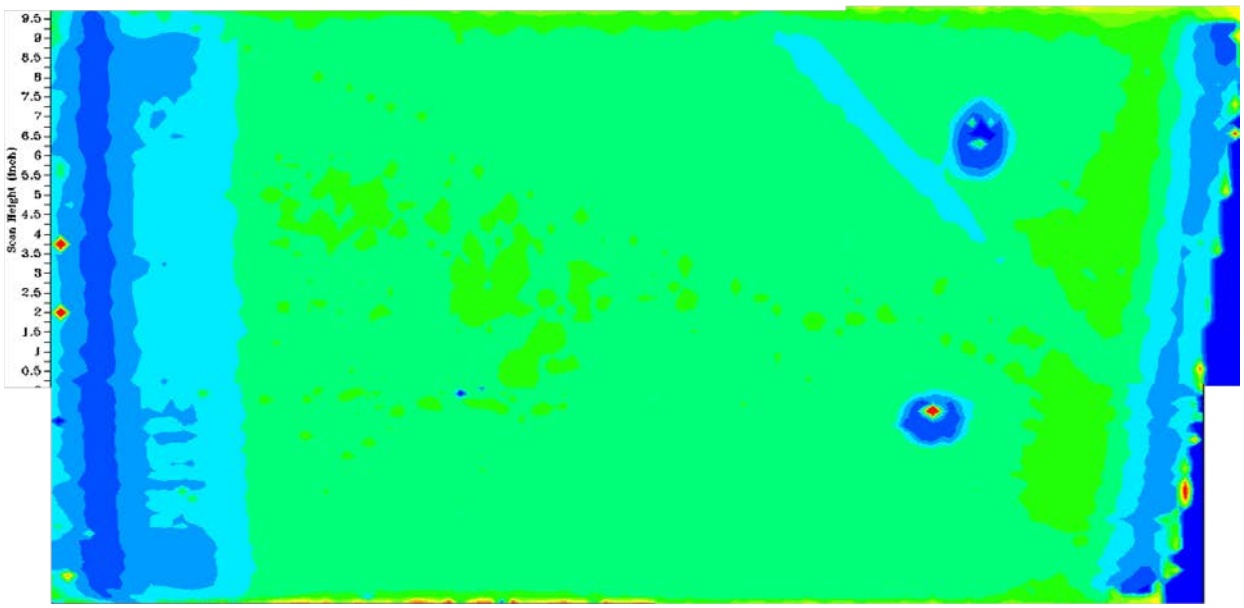

Figure 16. Delta Sample A: CATT Tau C-Scan Showing Local Variation in the Sample (note the previously identified fastener holes in the part and ply overlay areas.)

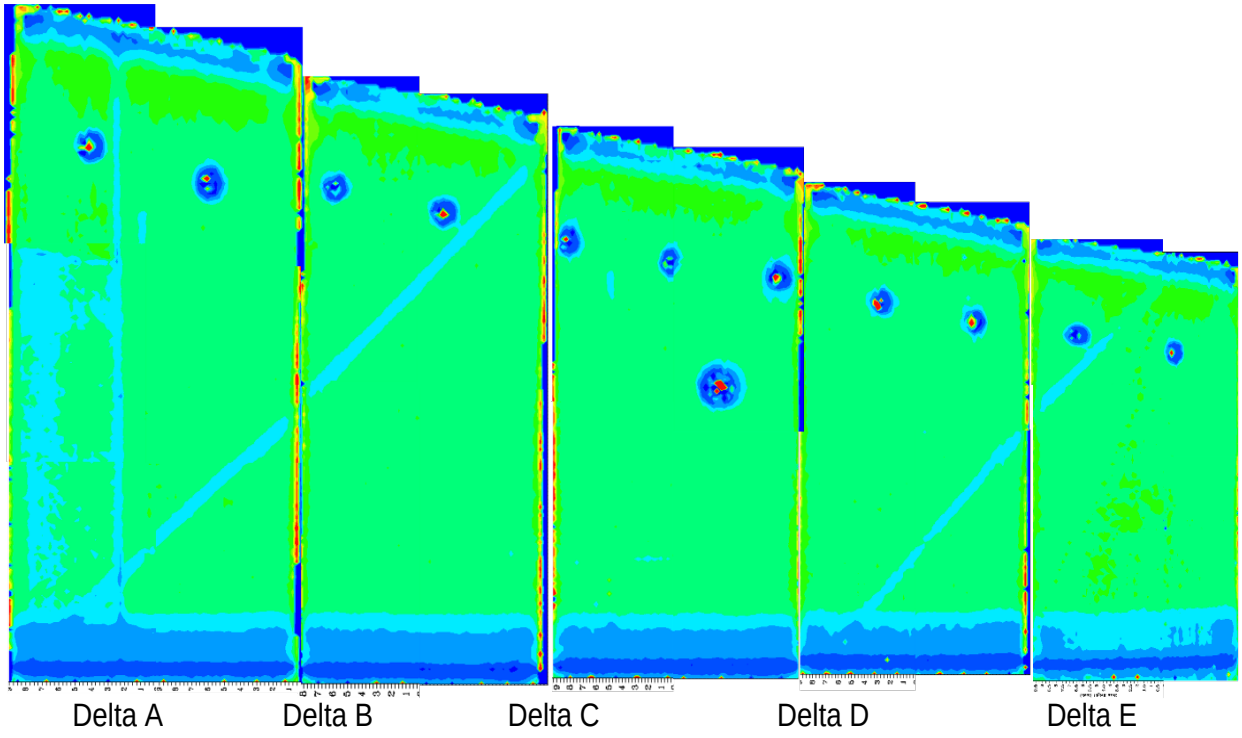

Figure 17. Delta Samples A–E: CATT Tau C-Scans Showing Local Variation in the Sample, but No Prior Damage and Uniform Central Regions for Impact Tests

3.4.3 Damage Via Impact.

The Instron 8200 drop tower was used to apply impact damage to the rudder samples. Initial tests were made to determine drop heights appropriate for the rudder design. Because the samples were too wide to fit between the carriage guide rods, the samples were held beneath the impact tower "table" and held rigidly in place using a hydraulic jack and thick composite plate. The drop tower impactor was attached to an extension rod to allow "through-the-table" impacts, as described in the Instron literature. Impact data were captured to ensure consistent impact energies and all impacts at a particular energy level were nominally within 10% of the predicted values.

3.4.4 Post-Impact Inspection—CATT.

Images produced by the CATT of post-impact damage demonstrated sensitivity typical of the instrument, identifying all the impact locations on each rudder sample. Shown are representative results on sample "A" and a mosaic of all samples Delta A–E in figures 18 and 19, respectively. Note that with decreasing impact energy (sample A>B>C>D>E), the damage size/area decreases. The CATT data were analyzed in the CATT software using the thresholding feature, allowing determination of damage area and equivalent flaw diameter for comparison to other post-inspection modalities.

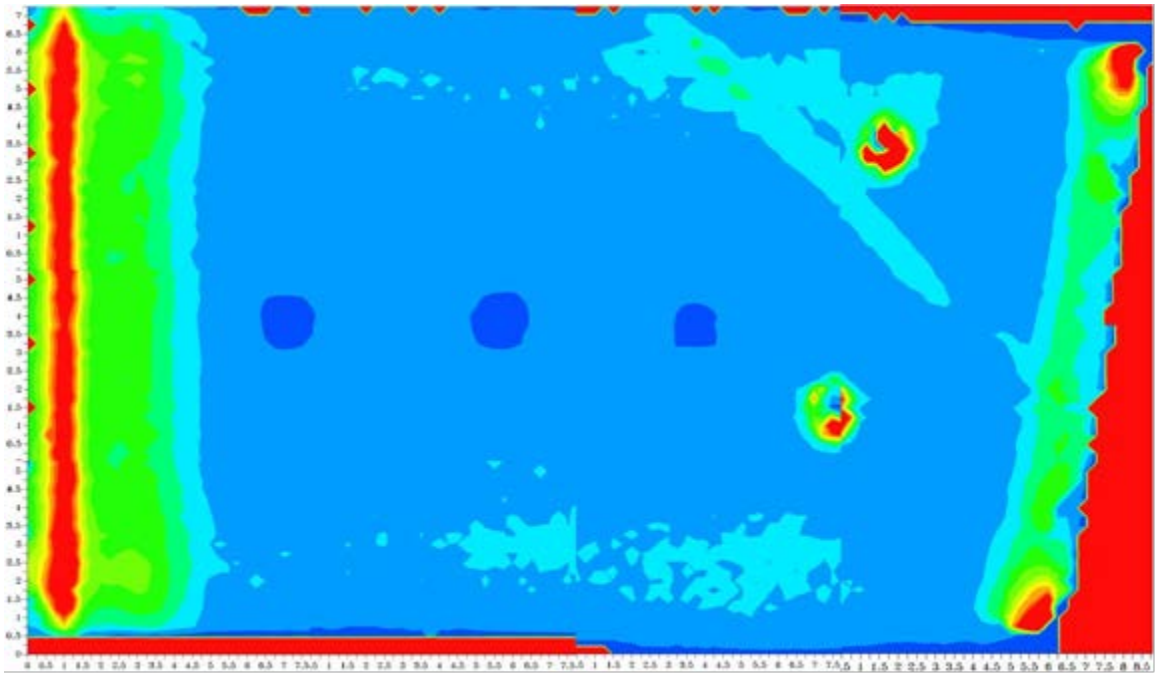

Figure 18. Sample A—Post-Impact CATT C-Scan Showing Damage Areas

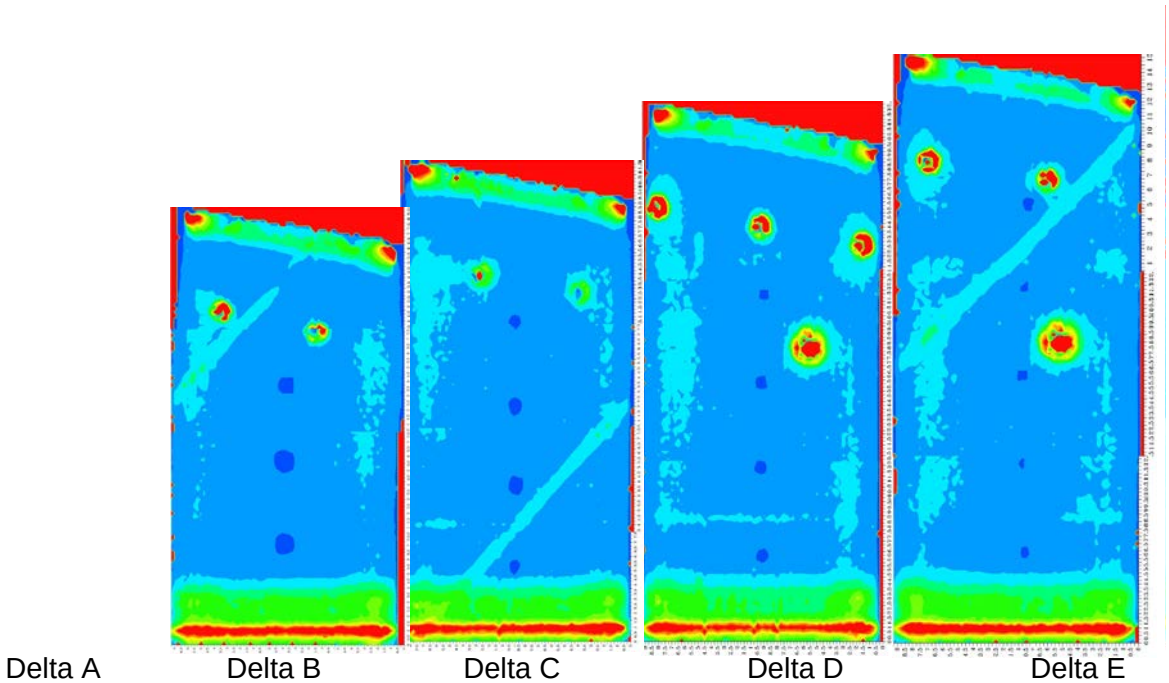

Figure 19. Mosaic of Samples A–E, From CATT Scan Images, Showing Internal Structure and Impact Damage

3.4.5 Post-Impact Inspection—ACUT.

Post-impact ACUT C-scans were made on each rudder sample. Shown again are examples of sample "A" and a sample mosaic in figures 20 and 21, respectively. With these post–impact ACUT scans, only the central region of the sample containing the impact sites were scanned to minimize scan time, but each resulting scan image is shown superimposed on the full pre-impact scans to provide an idea of impact location and size. Again, note decrease in damage site size/area with the correlating decreasing impact energy. The UTEX Winspect® software used to scan the samples incorporates a measure feature for which the operator can place the computer's cursor on features of an image and measure the distance between the features, which allows the direct measurement of flaw diameters. Horizontal and vertical flaw diameters were measured for each flaw on the samples and averaged for each sample to produce an average damage diameter for each of the impact energies employed.

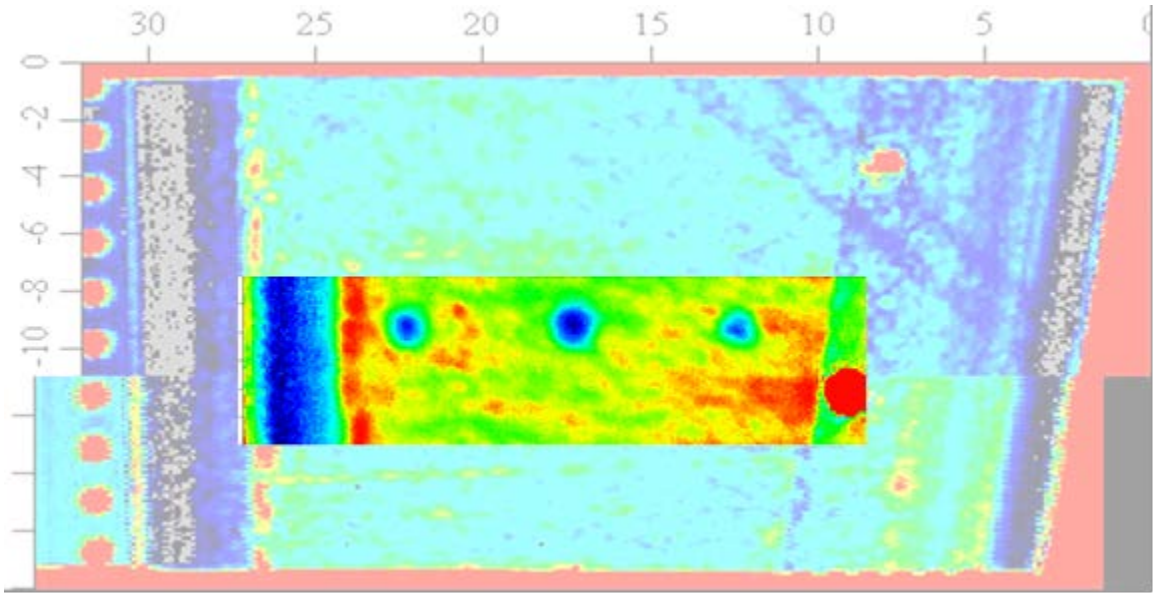

Figure 20. A 120 kHz ACUT C-Scan of Impact Damage Region on Sample Superimposed on Full Scan

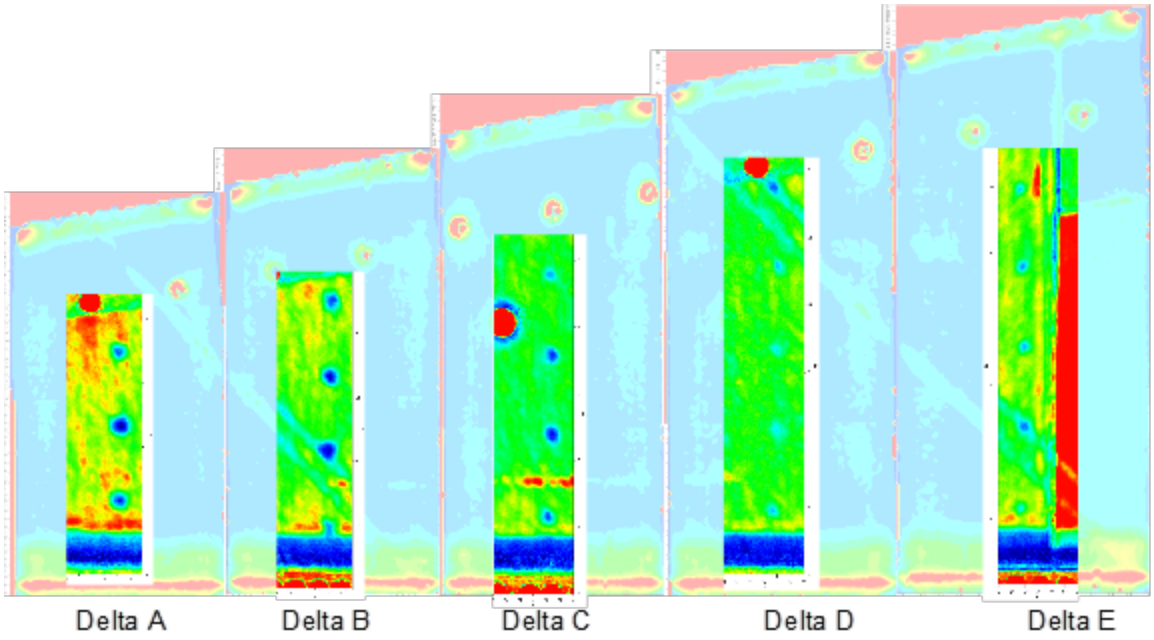

Figure 21. Mosaic of 120 kHz ACUT Scans Over Damage Region on Samples A–E Superimposed on Full Scans

3.4.6 Post-Impact Inspection—Sine Reference Method.

SRDA data in the form of C-scan images and data of post-impact damage were collected for each impact site on the samples. Data were collected via the GenScan software, which archived images and data from a 6″x6″ scan nominally centered over the impact area. The data collected from the GenScan were modified to allow analysis in the standard CATT software or Microsoft® Excel®, for which the damage size was characterized using a thresholding method and produced an equivalent damage diameter for comparison to the other post-impact inspections. Figure 22(a) shows a representative C-scan (raw bitmapped image, no processing) from impact site #1 on sample "A," with figure 22(b) demonstrating the results of processing the same data via thresholding to delineate the flaw area. Figure 23 shows the results from all the impact sites.

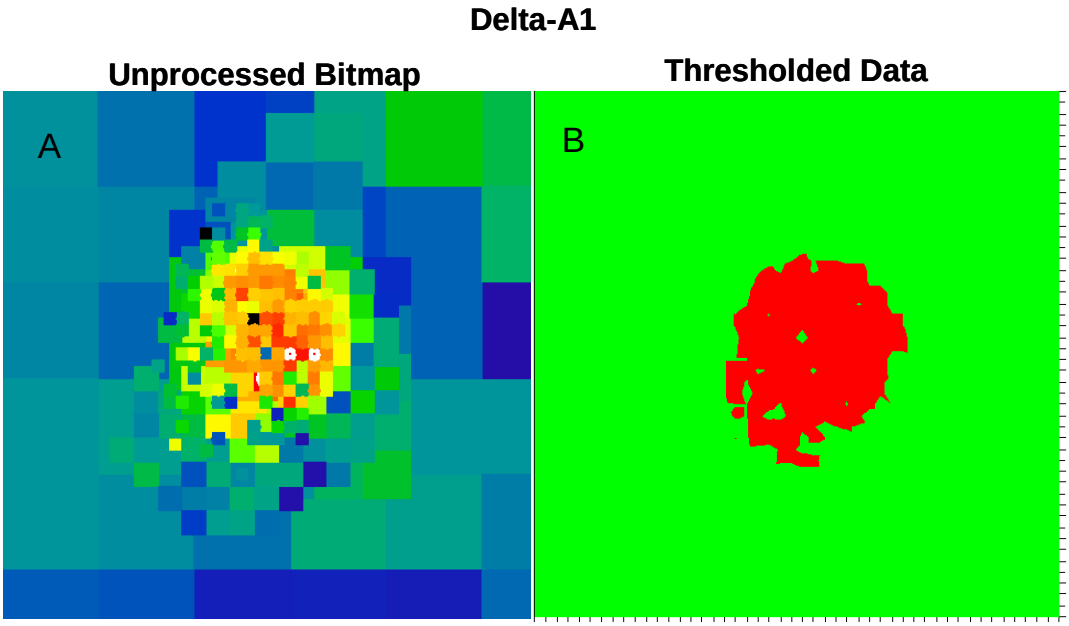

Figure 22. (a) Unprocessed SRDA Scan and (b) Threshold Image Delineating Flaw Region

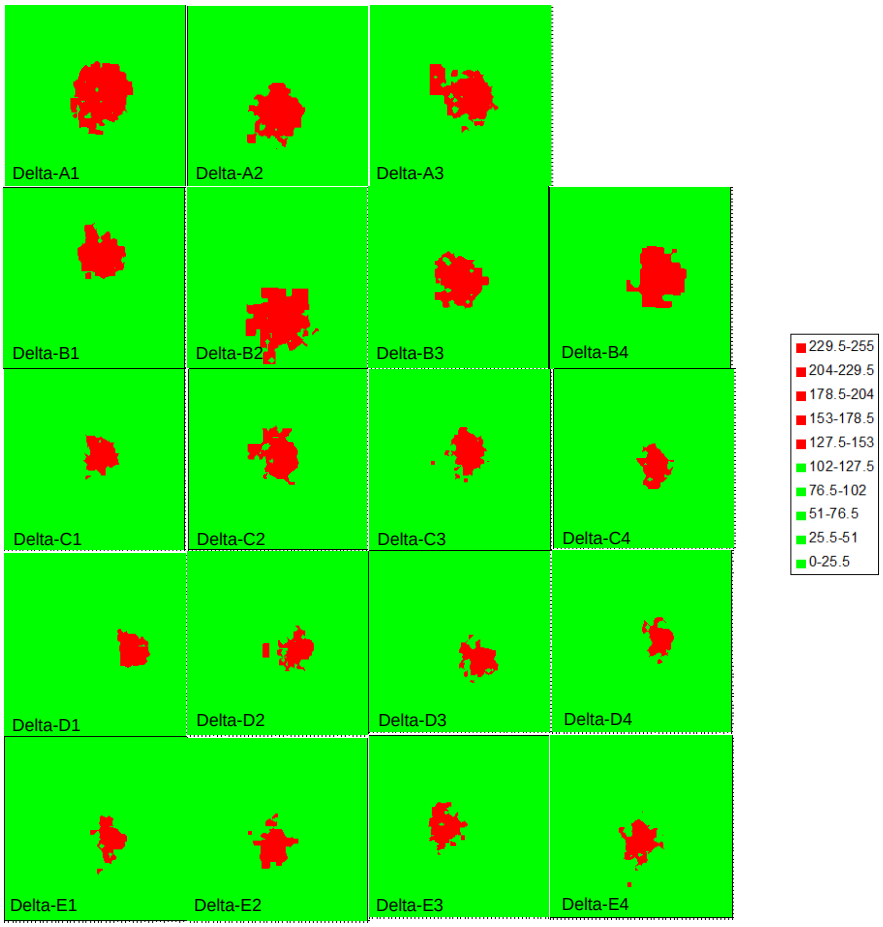

Figure 23. Threshold Images for All Impact Sites, All Samples

3.5 RESULTS AND ANALYSIS.

Post-impact inspections revealed all the impact locations and the size decrease of these areas with decreased impact energy. However, with decreasing impact energy, the contrast between damaged and undamaged areas decreased and the nominal variation in the sample tended to obscure the boundary between damage and nondamage. This is particularly noticeable in the ACUT results from samples B and E in figure 21, in which an impact site was placed on a ply overlay. Results from the post-impact inspections are summarized in figure 24, showing the measured average equivalent flaw diameter for the samples. The average equivalent flaw diameter is determined, in both CATT and sine reference methods, by first summing the pixel area above a particular threshold and converting this value to an equivalent diameter assuming a circular flaw area. In the ACUT results, the average equivalent flaw diameter is determined from the average of five vertical and horizontal measurements using the scan software measure tool, as described earlier.

The results demonstrate that each inspection method does a reasonably good job at characterizing the extent to which areas are damaged. The sine reference method consistently sized the damage area the largest, although without destructively sectioning the samples, the true size of the damage areas are ultimately unknown. However, the sine reference method also

appeared to reach a lower limit on sensitivity, because the equivalent diameters for the three lower impact energy levels were similar and not monotonically decreasing, as would be expected. In fact, the only inspection method that demonstrated a monotonically decreasing trend in flaw size with decreasing impact energy was the standard tap test (i.e., CATT). Additionally, the pixel sizes for these methods were not equal, with the pixel sizes for the ACUT, SRDA, and CATT data being measured at 0.08 inch, 0.125 inch, and 0.25 inch, respectively, so any underestimation of the flaw size increased with pixel size. In order to differentiate the sensitivity of the CATT and the hysteresis loop area/SRDA method without the influence of different pixel spacing, additional tests were conducted with a pendulum fixture.

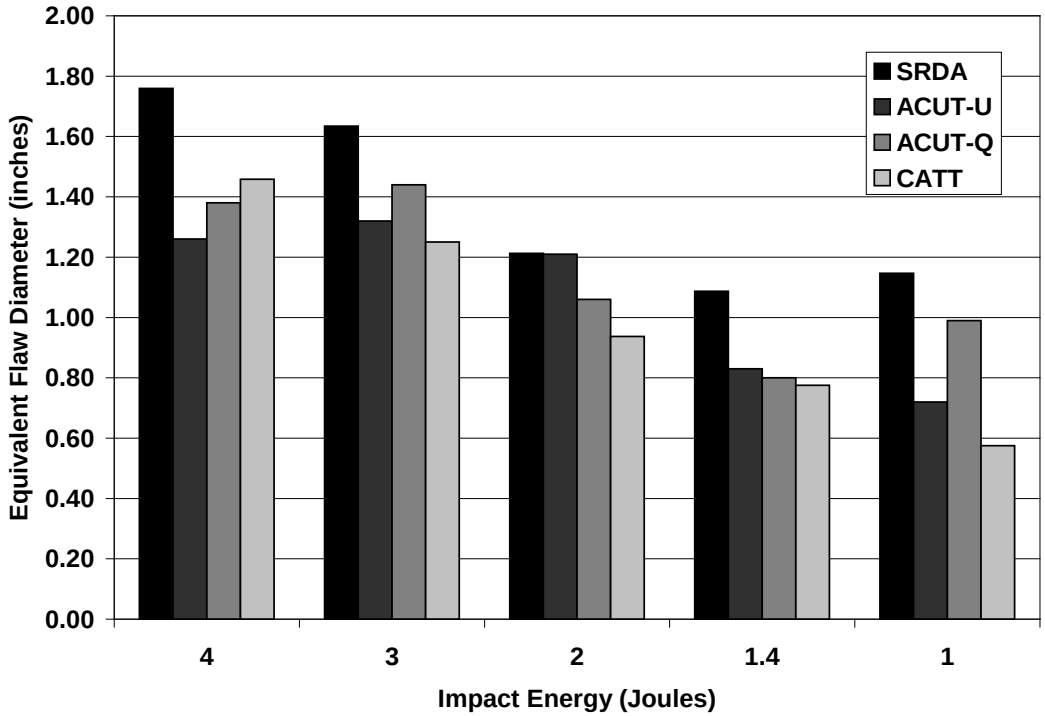

Figure 24. Equivalent Flaw Size as Determined From the Noted Inspection Modalities for Various Impact Energies

3.5.1 Additional Post-Impact Inspection—Pendulum Tapping.

A pendulum tapping fixture was fabricated to allow collection of very stable, consistent tap data. This pendulum tapper was manually operated, with an adjustable stop to fix drop height (and, therefore, the velocity at impact). Data was collected on a digital storage oscilloscope and transferred to a computer for analysis. With this data (the most consistent tap data available), several parameters were processed to evaluate the sensitivity of each to the impact damage. Data parameters included Tau, hysteresis loop area, SRDA, peak acceleration, and the damping coefficient, α (essentially a measurement of "Q" in the time domain, the ratio of the width of the acceleration curve at half max amplitude to the time to max amplitude). Figure 25 shows the pendulum tapper fixture.

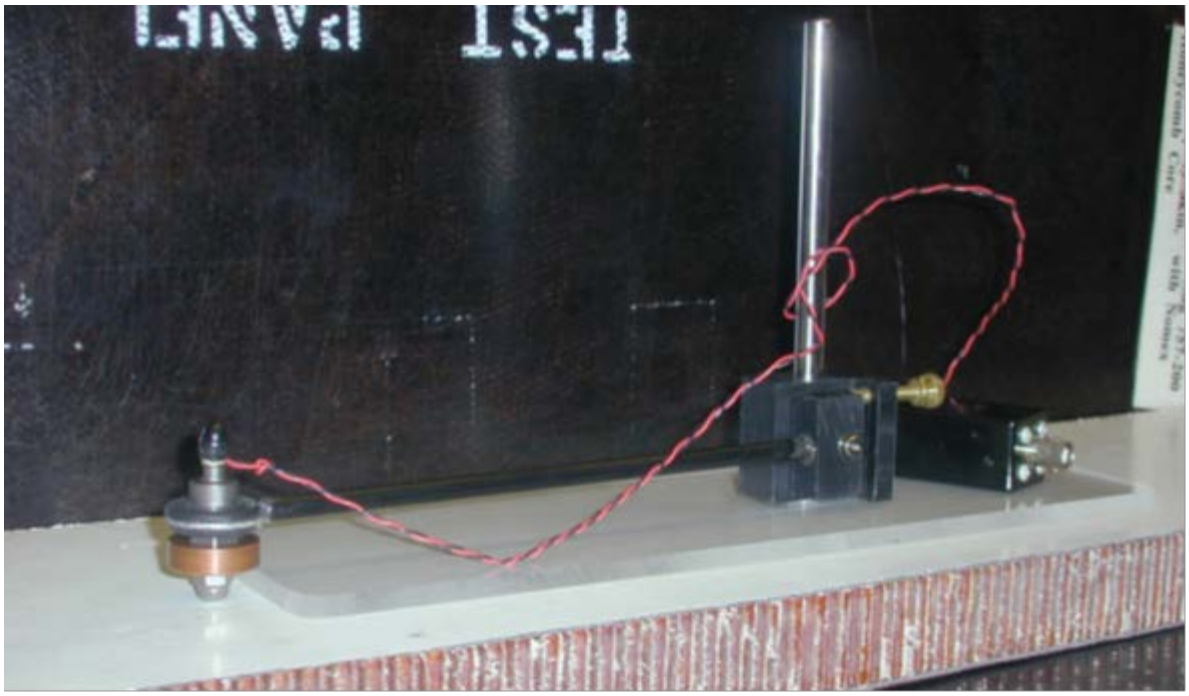

Figure 25. Pendulum Tapping Fixture Used for Collection of Very Stable Tap Data

For each rudder sample, the pendulum fixture was used to collect data tapping across the flaw sites, horizontally and vertically, collecting data every 0.125 inches along a path 4 inches in length, with the approximate flaw center at the 2-inch location. For each data point, the above noted parameters were calculated. Figure 26 (a and b) presents example results for hysteresis loop area versus position, averaged for each impact energy. Note that the data was "folded" about the center of the flaw, so the graphs show the average for each location with respect to the center, regardless of whether the tap path was vertically or horizontally oriented. Figure 26(a) shows the raw hysteresis loops, with 26(b) showing the normalized response (i.e., the response normalized to the value at a distance of 2 inches from the flaw, undamaged). Figures 27–30, show the normalized responses of Tau, SRDA, peak acceleration, and α. Of particular interest is the normalized response for each parameter at the center of each impact and on undamaged material. For all parameters, the normalized peak response at the impact center is in the range of 1.5 to 2 times that of an undamaged region (note that peak acceleration decreases over damage, whereas all the other parameters increase although the ratios are consistent). This would indicate that all the parameters measured, particularly the loop area, SRDA, and Tau, have similar sensitivity to damage, which is inconsistent with previous results. Earlier results indicated that loop area might be useful for further differentiating damage as compared to the standard tap test measurement of Tau, but these results suggest otherwise, at least in the case of the components used in these measurements.

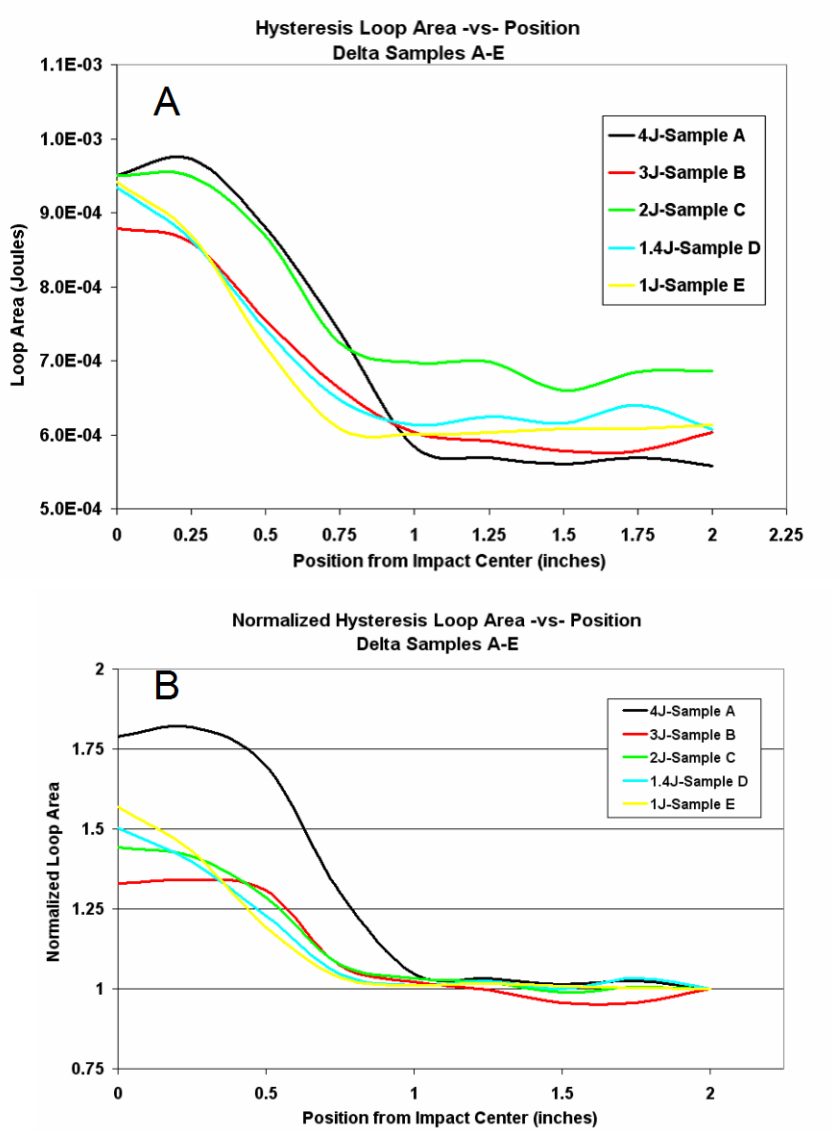

Figure 26. (a) Hysteresis Loop Area and (b) Normalized Hysteresis Loop Area vs. Position With Respect to Flaw Center

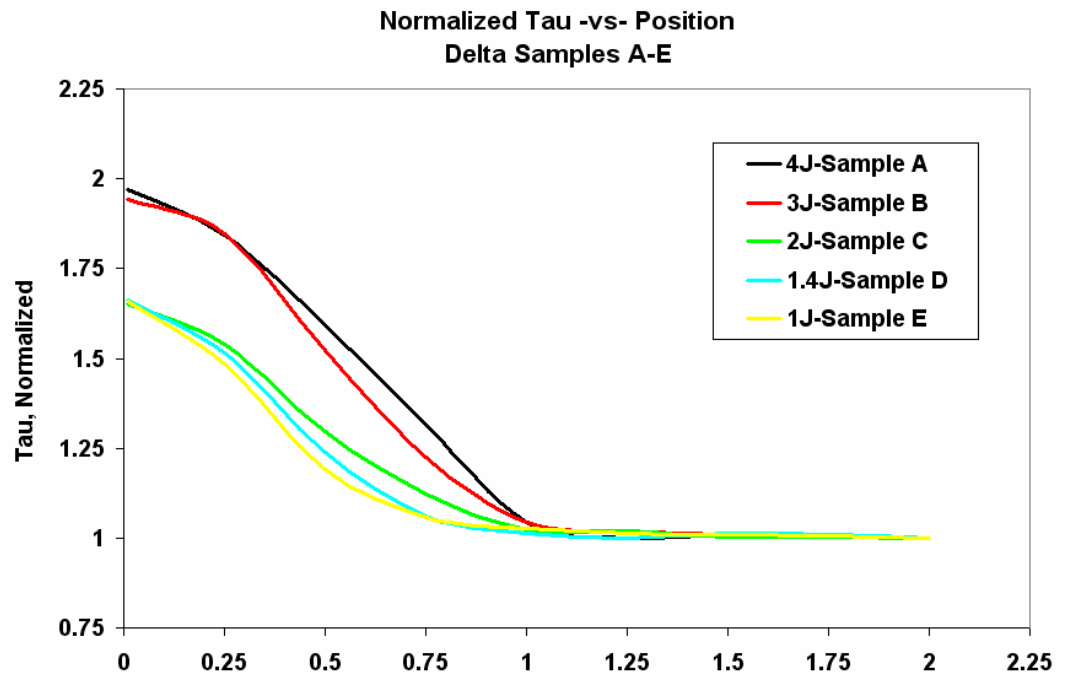

Figure 27. Normalized Tau vs. Position With Respect to Flaw Center

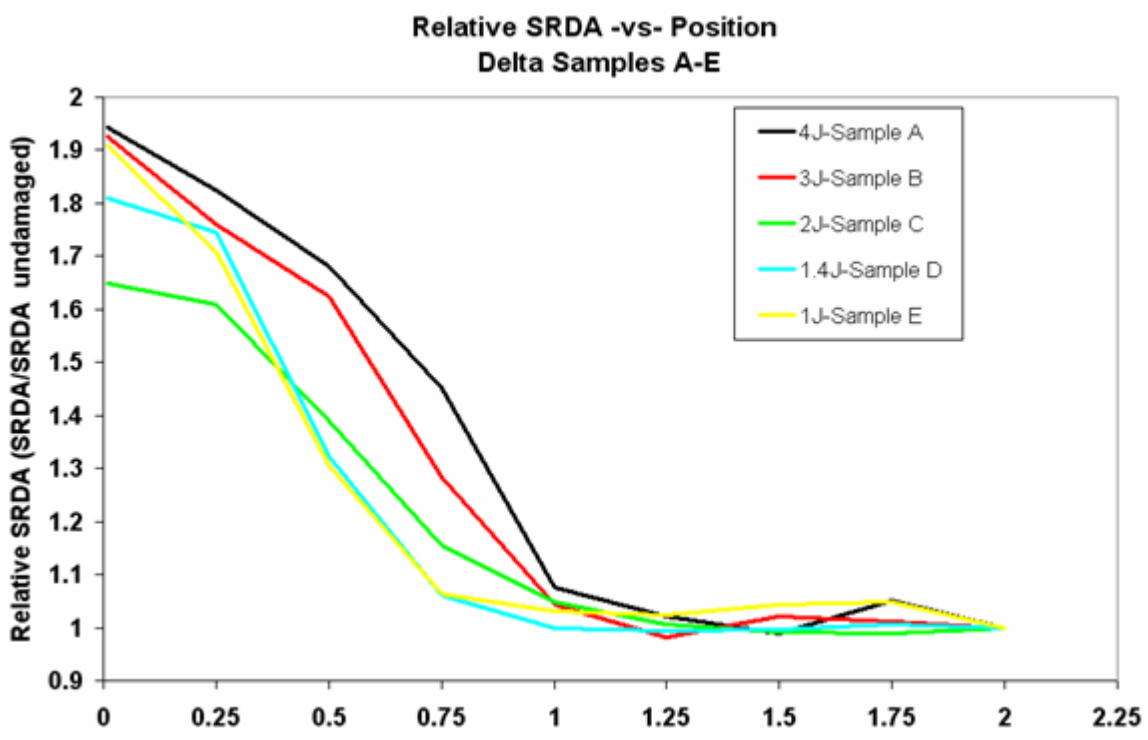

Figure 28. Normalized SRDA vs. Position With Respect to Flaw Center

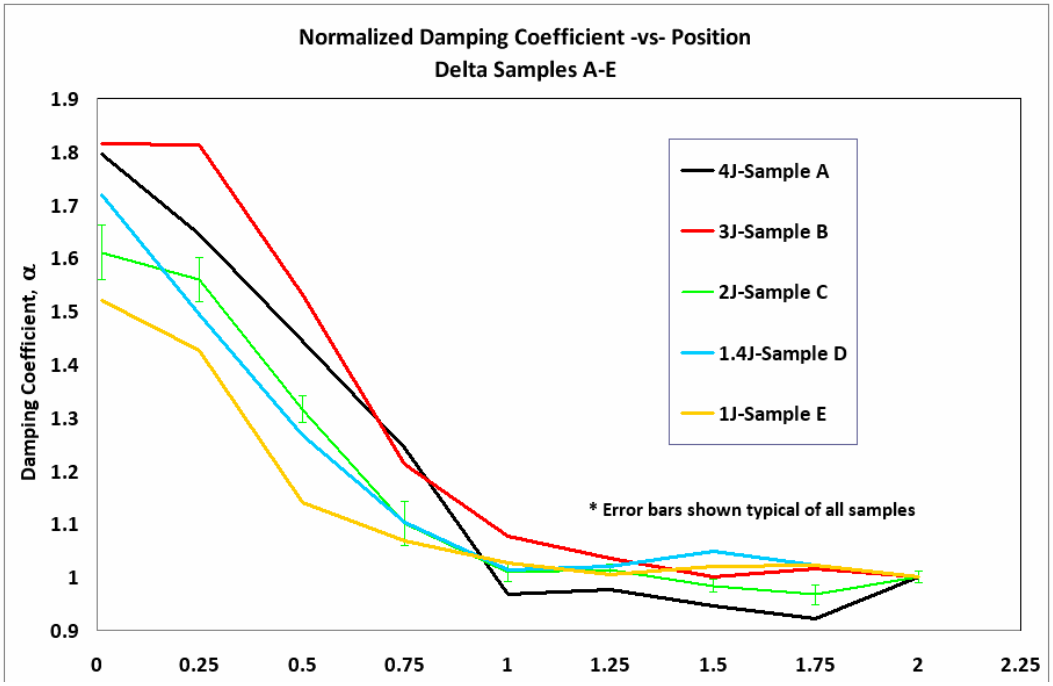

Figure 29. Normalized Damping Coefficient vs. Position With Respect to Flaw Center

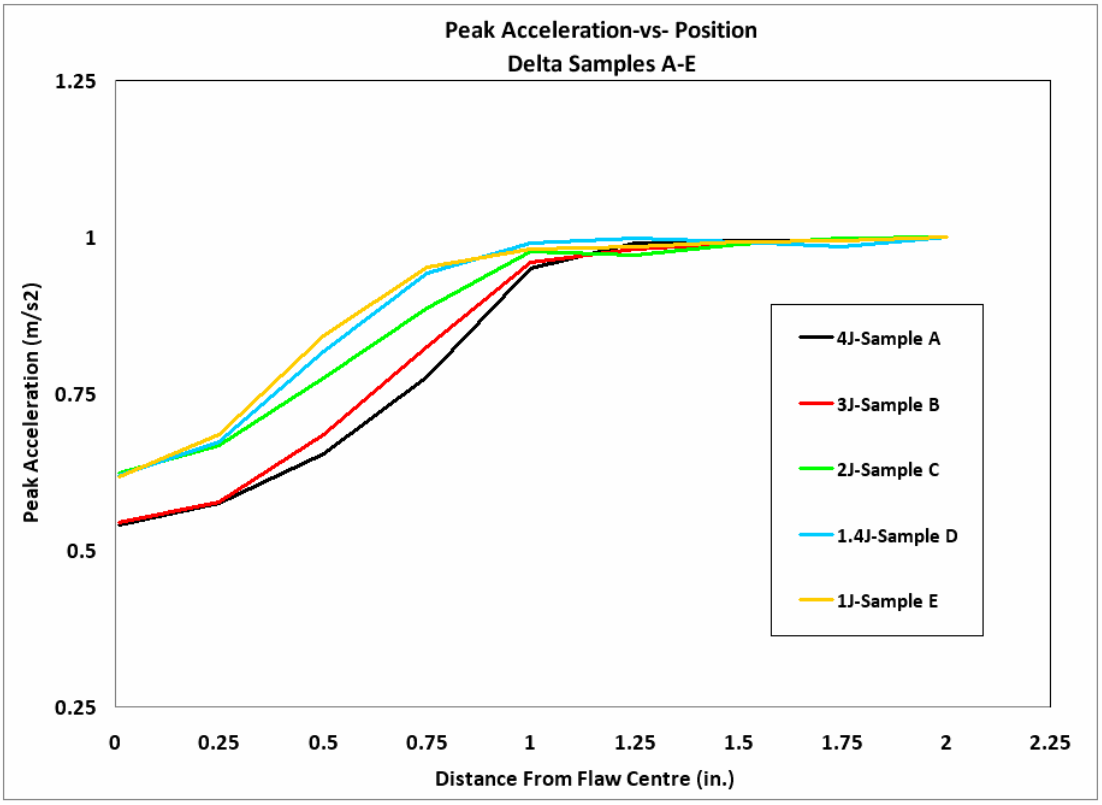

Figure 30. Normalized Peak Acceleration vs. Position With Respect to Flaw Center

As noted, earlier results indicated an expected increased sensitivity when evaluating the parameters that represent material nonlinear response, such as hysteresis loop area. However, for all nonlinear responses, high amplitudes are always involved. It is when a material is driven out of its linear regime that nonlinear responses manifest themselves. This is the case for mechanical, electrical, and magnetic responses (e.g., in magnetization, the material must first be driven into saturation before hysteretic response is seen). It is believed that this could be responsible for the lack of enhanced sensitivity of both the loop area and SRDA in these tests, in which a lightweight accelerometer is used as the tapping mass and is accelerated through a millimeter or so before contact with the part. In the initial dynamic loop area tests, the total tapping mass was in the order of 200 grams versus the 10–15 gram mass used in the these tests.

An important question to ask is whether, with increased mass, these dynamic hysteresis/sine reference methods could deliver increased sensitivity to impact in H/C laminate. When considering the results of the earlier dynamic tests, it is likely that increased mass would help, but it might also be expected that additional damage could result from the increased force of each tap. Additionally, simply increasing the mass is not a straightforward application because the mechanical components required to lift and accelerate the mass toward the part surface would need redesigning and the current motorized tapper would not be able to handle the additional loadings. Likewise, if the mass in increased, the tap durations would be longer, resulting in a requirement to significantly slow down the tap rate.

In summary, all the parameters derived from an accelerometer-based tap do a reasonably good job at differentiating damage and nondamage areas. At the low-force input ranges delivered by standard hand tap and motorized tap test equipment, very low levels of nonlinear (i.e., hysteretic) response are seen and, in general, appear to trend similarly to the linear response (i.e., Tau).

4. EXPLORATION OF NDI FOR SOLID LAMINATES.

4.1 MOTIVATION.

The main thrust of this project, funded by the FAA, was the development of an inspection technique based on the mechanical hysteresis of a structure and the change of hysteretic response when the structure is damaged. Hysteresis is most evident in structures that have a certain amount of flexibility, such as H/C sandwich structures and unsupported thin composite laminates. In the past, most of the attention on composite NDI was focused on H/C structures because of their wide use on aircraft and tendency to suffer impact damage. In recent years, however, more and more thick solid laminate structures are incorporated into primary, load-bearing aircraft structures. On the new generation of aircraft, such as the Boeing 787, almost all of the exposed surface of the aircraft's fuselage, empennage, and wings are made of carbon composite material; accordingly, the need for detecting and evaluating natural and human-caused damage to laminates has increased significantly. To adapt to the new world of composite airplanes, the NDI technology must evolve accordingly. For this reason, a number of explorations were pursued, aimed at advancing the inspection technology of solid composite laminates.

4.2 BACKGROUND OF NDI FOR SOLID LAMINATES.

Before describing the investigation of NDI for solid laminates, it is useful to review some facts regarding composite usage on aircraft. The percentages pertaining to composites by weight on some major models of airplanes are as follows: 10% on the B777, 25% on the A380, 33% on the A350, and 50% on the B787. The Boeing 787 uses very few H/C sandwich structures, except in its engine nacelle and winglet. Thick solid laminates of carbon fiber composites are used on both Boeing and Airbus airplanes as primary structures. The repair of these composite fuselage and wing structures entails a through-thickness bolted repair technique. The airlines have dealt with composite structures for more than 20 years, but the amount of composites on aircraft has made a quantum jump with the B787—and the NDI focus has broadened to include load-bearing primary structures.

The main concern for solid laminates remains the BVID. The most significant development reflecting the increased NDI need for solid laminates is the joint effort between Boeing Company and General Electric Sensing and Inspection Technologies, which resulted in the instrument known as the Bondtracer, and between Boeing Company and Olympus NDT, which resulted in the instrument 35RDC Ramp Damage Checker. Both are simple handheld ultrasonic instruments designed for preliminary screening of aircraft composites to identify areas of possible subsurface impact damage, normally used with a 5 MHz broadband contact transducer on composites with a thickness of up to 0.90 inch (23 mm). Both are basically a Go/No-Go ultrasonic gauge that airline ground personnel without NDT training, including luggage handlers, can use for making cursory checks of suspected damage. Neither is intended to replace comprehensive testing by a trained operator using an ultrasonic flaw detector. With the new generation of composite airplanes coming online, more sophisticated NDI techniques are clearly required to address the needs of ensuring structural integrity of solid laminate structures. This will include the development of ultrasonic techniques compatible with the field environment (one-sided, noncontact inspection) and techniques that are not ultrasonic in nature. To help the in-depth understanding of damage tolerance and failure mechanisms, it is especially necessary to investigate the microscopic morphology of subsurface impact damage and its growth and propagation under load.

4.2.1 Tap Test Using Heavier Mass.

The tap test is the time-proven technique for NDI of composite H/C structures because of the pliable nature of the facesheet. Solid laminates of composites, on the other hand, are much more rigid and, thus, not amenable to tap testing. It seems logical that the rigid solid laminate might require a larger mass to deform in a tap test; however, this was not borne out by experimental evidence. On the contrary, test results showed that the sensitivity for detecting a defect actually diminishes with increasing tapping mass. Quantitative tests were carried out on a 1/2-inch thick glass/polyester laminate with flat-bottom hole (FBH) defects. The contact time (τ) on and off an 1/8-inch deep, 1-inch diameter FBH on the back side of the 0.05-inch composite—using different masses from about 1 oz. to 4 oz—is shown in figure 31. The results showed decreasing detection sensitivity with increasing mass. It should be pointed out, however, that the presence of a rather shallow FBH did make a difference in the value of tap test contact time using a small mass.

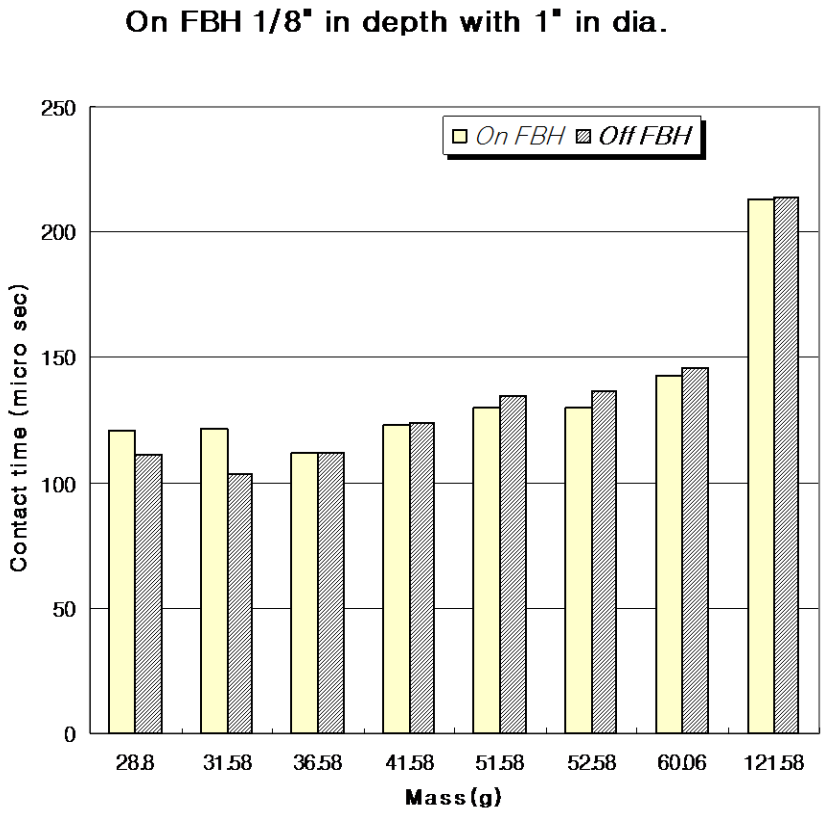

Figure 31. Contact Time as a Function of Tapping Mass for Composite Solid Laminates

4.2.2 Exploration of Composite NDI Using Acoustic Spectrum of Tap Test.

The physical basis for an instrumented tap test is the mechanical response of the structure to the tapping of a mass; this is measured in terms of the contact time between the mass and surface. A damaged structure is invariably less stiff and offers a longer contact time. In manual- and hearing-based tap tests, the operator judges the condition of the structure by the sound it makes when tapped. Therefore, it is instructive to examine the acoustic spectrum of a tap. A series of tests were conducted using a microphone and a spectrum analyzer to detect the differences between tapping on a good part and on a damaged part of several composite structures, including both solid laminates and H/C sandwich. The results showed that taps on composites produced acoustic signals all the way up to 25 kHz (above audio). This is contrasted to the equivalent frequency of 1 kHz to 5 kHz, corresponding to commonly measured contact time. A comparison of the acoustic spectra while tapping on a damaged region and an intact region often showed some differences, although they may occur at a different frequency region, depending on the damage and structure. Two examples are illustrated in figure 32, one for an H/C skin and the other for a solid laminate. The conclusion of the study was that acoustic spectrum can in principle be used in the evaluation of structural condition if the spectrum of a good part is available as a reference.

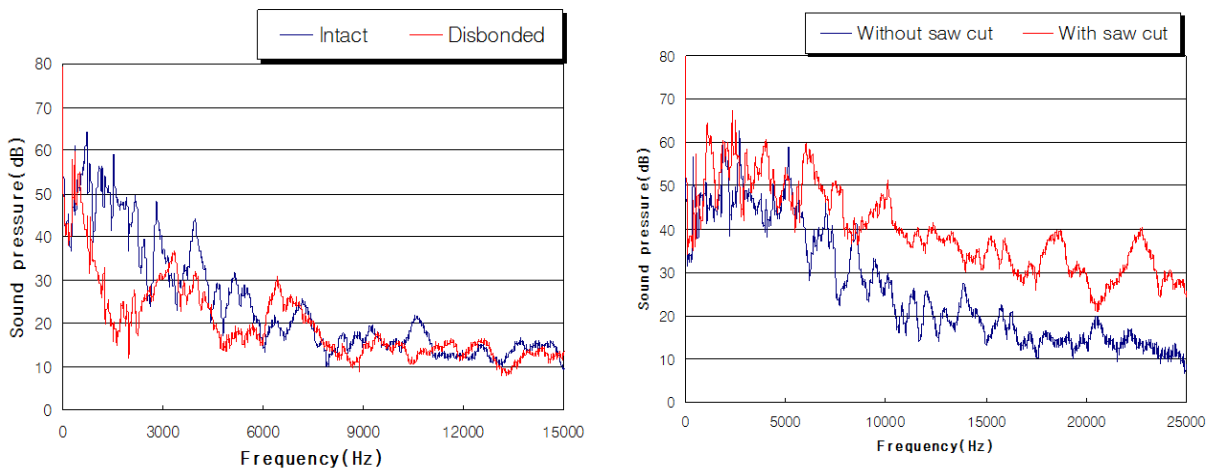

(a) (b)

Figure 32. (a) Acoustic Spectra of Tapping a Random Skin With a Half-Ounce Mass Over a Disbond and an Intact Region and (b) Acoustic Spectra of Tapping a 1/2-Inch-Thick Solid Laminate of Glass Composite on and off a Saw Cut at Its Mid-Plane

4.2.3 The NDI of Solid Laminates.

Composite solid laminates, typically without reinforcement in the out-of-plane direction, are prone to impact damage and the resulting delaminations. The BVID remains a major concern in the NDI of composites to this date. While the characteristics and NDT of impact-induced delaminations are well known, the precursor to failure in the form of microcracks has not received its deserved level of attention. The threshold of damage in solid laminates; the morphology of damage (especially the transition from matrix microcracking to ply delamination) and the progression and growth of damage under fatigue loading were investigated. The

detectability of the various stages of damage by ultrasound was investigated. The composites studied included solid laminates of carbon fiber reinforced polymeric composites and glass fiber reinforced composites fabricated from both woven and unidirectional prepregs.

4.2.3.1. Delamination Threshold of Impact Damage in Solid Laminates.

At impact energies above a certain threshold, the damage in composite solid laminates takes the form of a series of delaminations, often occurring in pairs at each ply interface, that increase in size at greater depth. This phenomenon is well documented and their detection and imaging by ultrasound has been quite successful. Previous results, included here in figure 33, showed the delamination pattern on a cross-sectional plane cut through the center of the impact damage and the corresponding ultrasonic C-scan image of the damage.

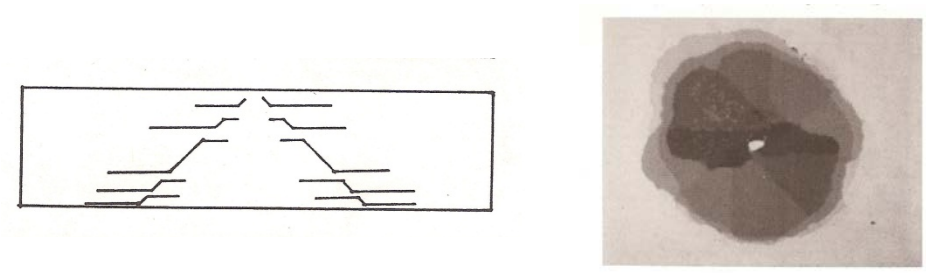

(a) (b)

Figure 33. (a) Schematic Diagram of Impact Damage on the Cross Section Plane and (b) Ultrasonic Image of the Delaminations Caused by Impact (Taken from Gosse and Hause, QNDE, 1988)

Of particular interest during this study was the damage morphology at energies below the delamination threshold. The pre-delamination damage was in the form of a volumetric distribution of microcracks in the resin matrix. The distribution density and orientation of the microcracks may be examined with optical microscopy on polished cross sections of the impact zone. Glass composite laminates were impacted first to take advantage of their translucent nature. Samples of solid laminates were impacted with increasing energy using an Instron Dynatup 8200 impact tester. The threshold for delamination in glass composite was easily determined by visual examination. Delaminations appeared as opaque regions, whereas pre-delamination microcracks appeared as a cloudy region, as shown in figure 34. Here, a 24-ply woven glass fiber reinforced plastic (GFRP) laminate (0.23-inch thick) was impacted with a hemispherical tup of 2-inch diameter with the sample held down on the platform of the impact tester over a 3-inch diameter hole. The total mass of the drop weight, including the mass of the carriage and the tup, was 3.34 kg. The threshold for delamination in this sample under the boundary conditions just described was approximately 10 Joules. Examination of impact results on a number of GFRP laminates showed that the onset of delamination as the impact energy increased was usually rather abrupt, in the sense that delaminations did not seem to occur below a certain minimum size. It should also be pointed out that the threshold of damage depends strongly on the size, geometry, and support condition. For example, a large composite fuselage barrel would require a much higher impact energy to inflict delamination.

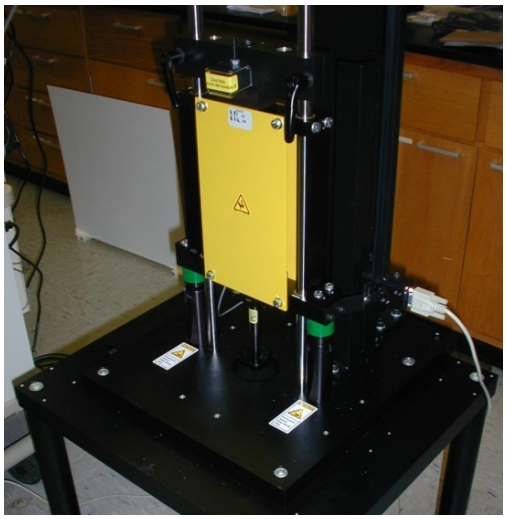

(a)

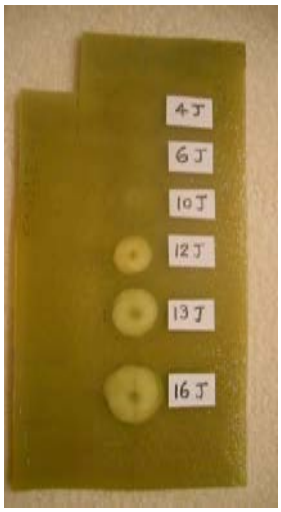

(b)

Figure 34. (a) Instron Dynatup 8200 Impact Tester and (b) Impact Damages Made on a 24-Ply Woven GFRP Solid Laminate at Different Impact Energies

The threshold of delamination in carbon composite laminates was also investigated. Because the carbon composites were totally opaque, ultrasound was used to monitor the results of impact at various energies. Using the same Instron impact tester, the onset of delamination of a 24-ply [0/90]12 laminate was found to occur at approximately 18.5 Joules. This specimen was a solid laminate fabricated from unidirectional prepreg tapes (i.e., it was not a woven composite). The specimen was impacted at 15, 17, 18, 18.5, 19, and 20 Joules of incident energy and the damages were examined with contact mode ultrasonic testing (UT) and immersion C-scan. At the energy corresponding to the onset of delamination, the changes were quite distinct. Below this energy, the damage zone was small (10 mm or less) and the effect of the damage on an ultrasonic beam was quite minimal. The back wall echo amplitude was attenuated by approximately 10%. Above the threshold energy, the diameter of the damage zone became typically 25 mm or larger and the delaminations completely blocked the back wall echo. Figure 35 shows the pulse-echo time-of-flight scan image, produced by a 5 MHz transducer, of the damage below the delamination threshold at 17 Joules and the damage at the threshold at 18.5 Joules.

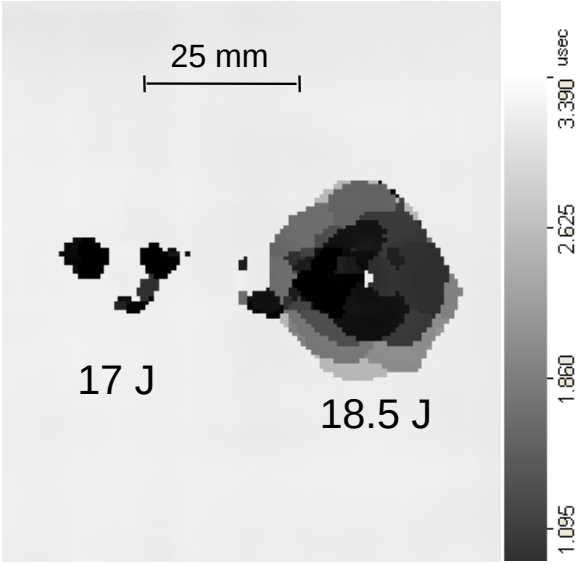

Figure 35. Time of Flight Immersion C-Scan Image of Impact Damage With Almost No Delamination (left, at 17 J) and One With Extensive Delamination (right, at 18.5 J)

4.2.3.2. Microscopic Morphology of Pre-Delamination Impact Damage.

To understand the nature of the state of damage at energies below the initiation of delamination, detailed microscopic examination of the low-energy impact zone in different carbon and glass composite laminates were carried out. The impact zone was sectioned, polished, and optically micrographed to examine and document the state of damage. Prior to the onset of delamination, the damage was primarily in the form of matrix microcracking. The crack density distribution and crack orientation were studied in the 24-ply woven GFRP laminate at impact energies below and near the delamination threshold. The spatial distribution of the crack density produced by impact energy of 9, 10, and 11 Joules is shown in figure 36. When the numbers in the squares represented the number of cracks per square millimeter; each square in the figure was 1 mm x 1 mm. The results showed that most of the cracks were located near the back surface and slightly away from the impact point.

The microcracks produced by impact were generally tilted. Those located to the left of the impact point tilted to the right (toward the impact point) and those located to the right of the impact point tilted to the left. This behavior was also observed in impact damage above the delamination threshold, where both delaminations and microcracks were present. Figure 37 shows the tilting of the microcracks at a 10-Joule impact site.

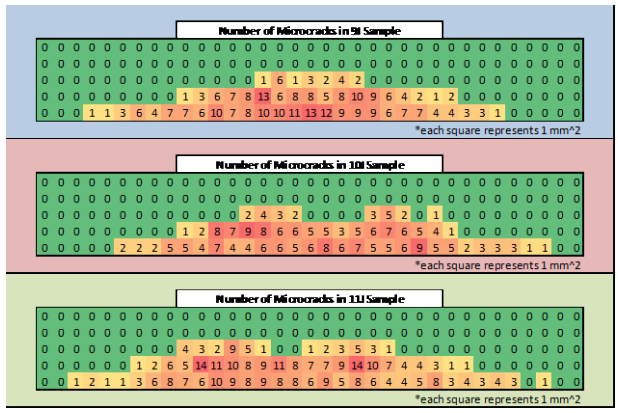

Figure 36. Spatial Distribution of Microcrack Density
Produced by Impact Energies of 9, 10, and 11 Joules

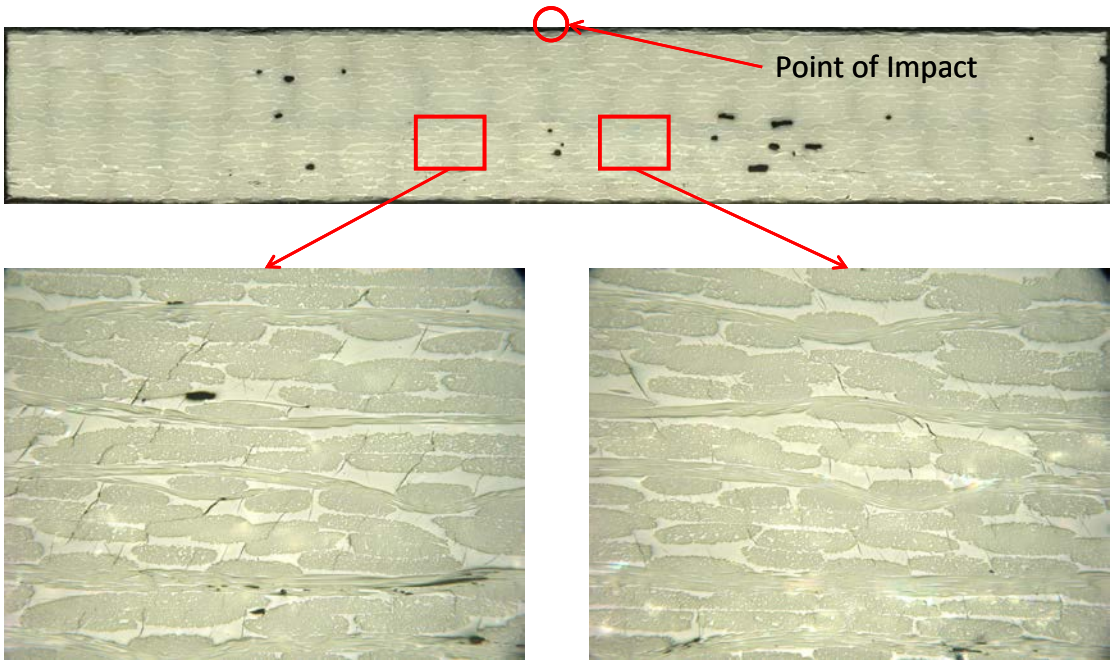

Figure 37. Microcracks in Woven GFRP Produced by an Impact With 10 Joules of Incident Energy (optical micrographs show that the microcracks (faint short fine lines) tilt toward the impact point)

4.2.3.3. Evolution of Microcracks Under Fatigue.

The initiation and growth of delaminations from impact-induced microcracks during the service life of load-bearing composite structures is a major concern to the industry. The actual engineering problems are exceedingly complicated and depend on numerous factors, including the material and construction of the composite and the magnitude and geometry of the stress environment. In the laboratory, it could be instructive to conduct fatigue tests of impact-damaged composite laminates to investigate the behavior of the microcracks under fatigue load in spite of the fact that the type and magnitude of load may not be realistic. With this in mind,

impacted solid laminates at energies below the delamination threshold were subjected to three-point bend fatigue tests to induce and grow delaminations. To observe the in situ changes during the fatigue process, samples sectioned through the center of the impact zone were tested and the cross-sectional surface was polished optically to observe the changes to the microcracks during fatigue. The tests were conducted on small samples using a short beam shear test fixture on an MTS machine.

During the fatigue test, many of the tilted microcracks were found to grow and deflect to the horizontal direction, thus producing micro-delaminations. Figure 38 shows the before and after fatigue comparison of a small region of a 10-Joule impact zone. The microcracks in the two images were identical, except that some short and tight delaminations appeared after 1000 cycles of fatigue. For example, the microcrack at the center of the micrograph appeared to have propagated downward and ran into the interface with a 0-degree ply, at which point it turned horizontally and continued to the left. The microcrack near the left end of the micrograph had propagated upward along fiber tows, jugged upward, and continued horizontally to the right. These micro-delaminations were much tighter and shorter than the interlaminar macro-delaminations caused by high-energy impact. The former attenuates an ultrasonic beam only slightly, whereas the latter can efficiently block an ultrasonic beam. In a woven composite, many of the delaminations between fiber tows remain localized because their propagation quickly becomes thwarted by other intervening fiber tows. However, when the fatigue test of the sample containing the micro-delaminations continued to a higher load, the sample eventually failed after producing numerous macro-delaminations at the interfaces between the woven plies. In a laminate fabricated with unidirectional prepregs, however, the growth of interlaminar delaminations during fatigue tended to propagate unimpeded.

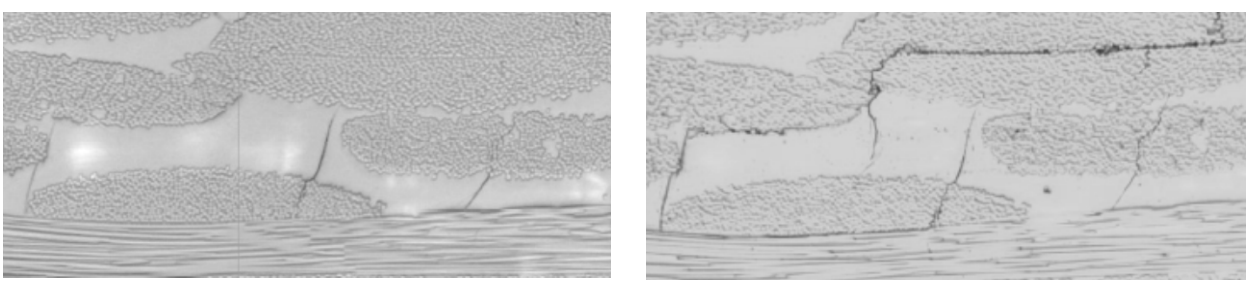

(a) (b)

Figure 38. A Small Region of the Cross Section of Impacted GFRP Laminate (a) Before and (b) After Fatigue Test

4.2.3.4. Ultrasonic Detection of Impact Damage.

The ultrasonic detectability of microcracks and delaminations associated with impact damage of composite laminates were investigated. The most significant finding was that delaminations caused directly by high-energy impact were easily detected with conventional pulse-echo contact mode UT, whereas delaminations grown during fatigue from microcracks produced by low-energy impact were not easily detectable with contact UT. The experimental results obtained on a woven glass epoxy laminate are summarized in figure 39. The micrograph and UT signal on the left belong to the high energy (16 Joules) impact damage and those on the right belong to the

low energy (9 Joules) impact damage followed by fatigue. For this glass composite, the threshold for delamination is an impact energy of approximately 11 Joules.

Careful microscopic examinations of the two types of delaminations—those produced directly by high-energy impact and those grown in fatigue test from low-impact energy microcracks—revealed several differences. Impact-induced delaminations (with impact energy above the delamination threshold) have large crack opening displacement (COD) (typically 10-20 microns) and occur between adjacent plies. Therefore, they are quite long and can reach many millimeters. These delaminations may be regarded as macro-delaminations. They can readily block an ultrasonic beam, as shown in figure 38. In contrast, the micro-delaminations that grew from matrix cracks during the fatigue test of a sample impacted at low energy (below delamination threshold) were much more tightly closed, with a COD on the order of 1 micron. They often occur within the woven ply between fiber tows. As a result, they are usually very short because their propagation is quickly thwarted by adjacent fiber tows. Ultrasound can propagate through a population of these micro-delaminations relatively unimpeded. The back-wall echo amplitude was measured through such a region and was found to be only slightly less (approximately 10%) than that of a pristine region.

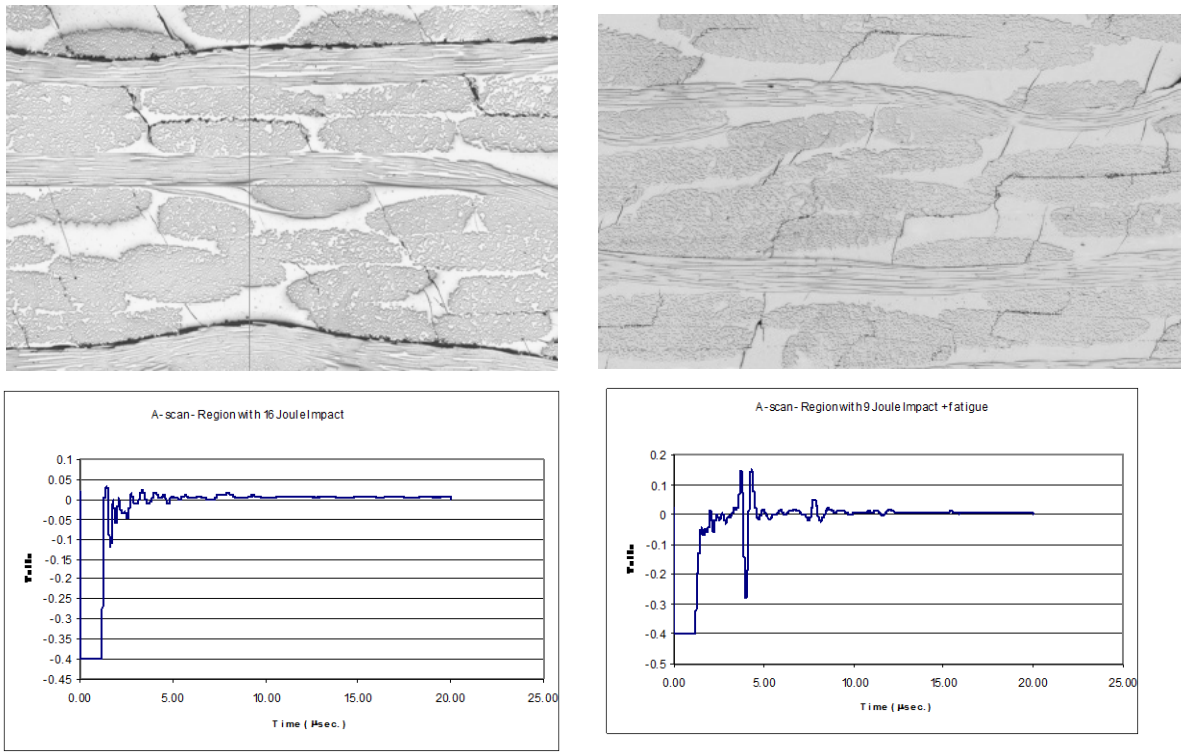

(a) (b)

Figure 39. (a) Delaminations With Large COD Produced by High Impact Energy of 16 J, Block the Ultrasonic Beam Efficiently (back wall echo invisible) and (b) Delaminations With Small COD and Short Length Grown From Microcracks During Fatigue Test Were Not Easily Detectable With Ultrasound (back wall echo only slightly reduced. Sample was a 24-Ply Woven Glass-Epoxy Solid Laminate.)

4.2.3.5. Impact Damage and Fatigue of Carbon Composite Laminate.

The findings pertaining to solid laminates of woven glass composites were described in sections 3.3 and 3.4. These findings on the damage morphology as a function of impact energy and the evolution of microcracks under fatigue served as useful guides in our study of the most relevant material system: solid laminates of carbon composites fabricated from unidirectional prepreg tapes.

A [0/90] 6S carbon composite laminate, 4.6-mm thick and fabricated from unidirectional prepreg tapes, was subjected to impact hits at different incident energy near the threshold for delamination. Specifically, 18-Joule impact produced mostly matrix microcracks and no delaminations. An 18.5-Joule impact produced matrix cracks as well as limited local delaminations. Fatigue test samples were cut from the impacted laminate and the edges were polished to optical finish for microscopic examination of their damage state. The 18.5-Joule sample was fatigue tested using a three-point bend fixture at a frequency of 5Hz and peak load of 671 lbf at $R = 0.1$. The fatigue was stopped periodically for optical microscopy of the damage state. The specimen was eventually tested to failure. The optical microscopy revealed the following significant findings:

- Under fatigue load, some matrix cracks began to widen and initiate delaminations, often in both directions, at the ply interface. Figure 40(a) shows a tilted microcrack in a 90° ply caused by a low-energy impact. During fatigue, its width increased and delaminations were initiated at the interfaces with the 0° plies above and below the microcrack. The delaminations were initially short and localized, but grew in length and width as the fatigue progressed. Figure 40(b) shows a delamination that had propagated in the resin-rich layer between two plies and grew to a width of about 50μm. Figure 41 is a closeup micrograph of a microcrack evolution during fatigue and shows a region of the polished cross-sectional surface before and after fatigue. The region is located to the right of the impact site, hence all the micrographs showed the widening of a number of microcracks and the initiation of delaminations at their ends.

- The delaminations grew in length with accumulating fatigue cycles and joined with delaminations at adjacent ply interfaces via the tilted microcracks. Eventually, the network of delaminations connected by left-tilting microcracks to the right of the impact site became connected with the network of delaminations to the left of the impact site, joined by the right-tilting microcracks. When a sufficient number of delaminations linked up and propagated, the specimen's ability to sustain load dropped precipitously and the specimen began to shed load and fail. Figure 42 shows the morphology of the impacted laminate described in figure 40 after failure in fatigue. The figure shows a zoomed-out view of the central portion of the sample. The sample was 4.6-mm thick and the impact point was at top center. This micrograph was taken at low magnification under a stereo-zoom microscope. The lighting was such that thick white lines are delaminations, thin tilted white lines are matrix cracks, and discontinuous strings of white dots are mostly light scattered from ply interfaces (without delaminations).

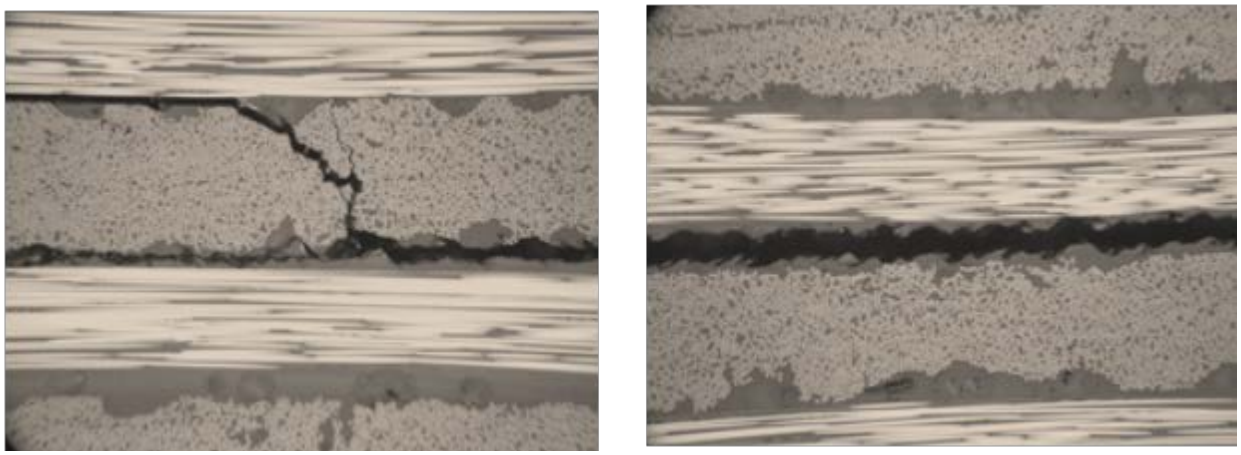

(a) (b)

Figure 40. (a) A Matrix Crack in a 90-Degree Ply Widened During Fatigue Test and Initiated Delaminations in Both Directions, and (b) the Propagation of a Wide Delamination (~50 microns) in a Resin Layer Between a 0-Degree Ply and 90-Degree Ply

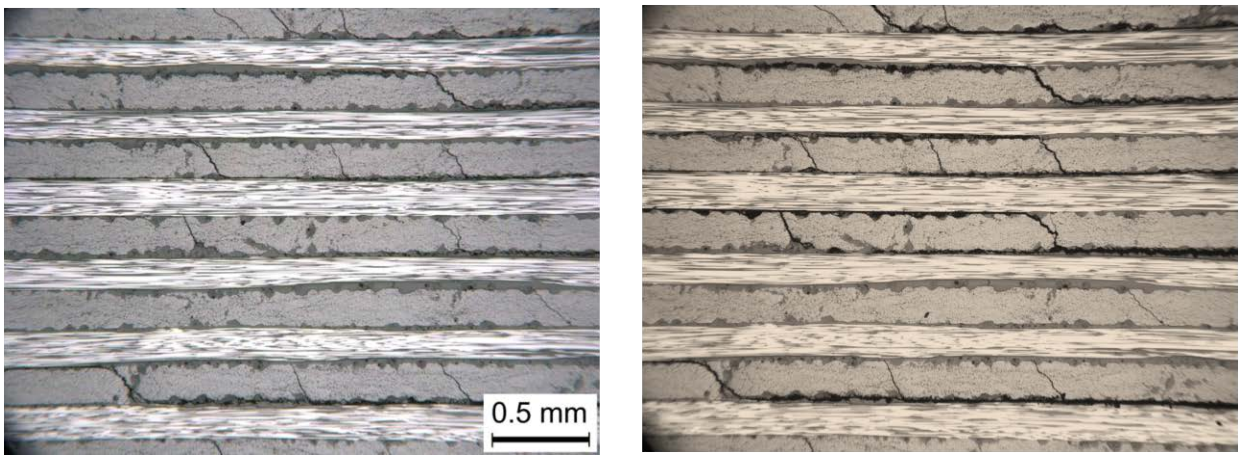

(a) (b)

Figure 41. Changes of Microcracks During Fatigue of a Region to the Right of an 18.5-Joule Impact in a 24-Ply [0/90] 6S Laminate of Carbon Composite (a) Before Fatigue and (b) After Fatigue (Darkening of the microcracks indicates an increase of the COD while some initiation of delaminations at their ends can be seen.)

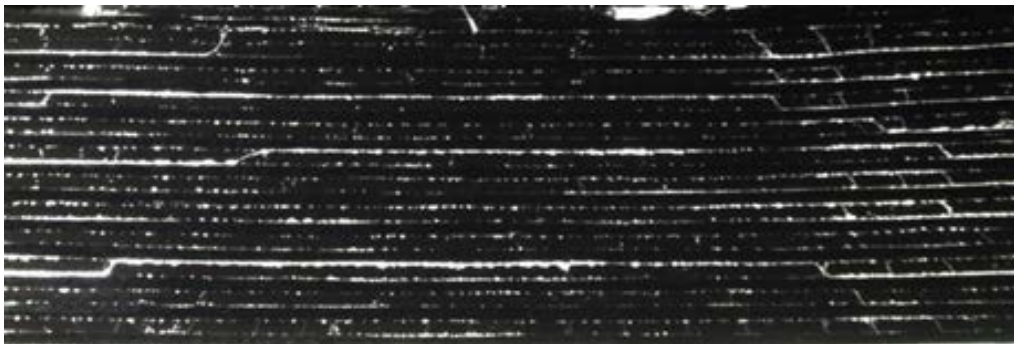

Figure 42. Morphology of an Impact-Damaged 24-Ply [0/90] 6S Laminate of Carbon Composite After Failure in Fatigue Test. (Notice the delaminations (dark white lines) at adjacent interfaces joined by the tilted microcracks.)

- The following description of the evolution of impact damage under fatigue is offered. When a low-energy impact damage zone containing only matrix cracking is subjected to fatigue loading, some of the matrix cracks begin to widen and initiate micro-delaminations in one or both directions, but initially of very limited length (hundreds of micrometers). As the fatigue continues, these micro-delaminations grow into macro-delaminations that are much longer (millimeters). Eventually, the jogs and delaminations on the left and right sides of the impact join up and propagate to lengths of centimeters. This leads to considerable reduction of the sample stiffness and load shedding during the fatigue test. If the testing were not stopped by preset interlock, the sample would have broken completely. Figure 43 shows the evolution process schematically.

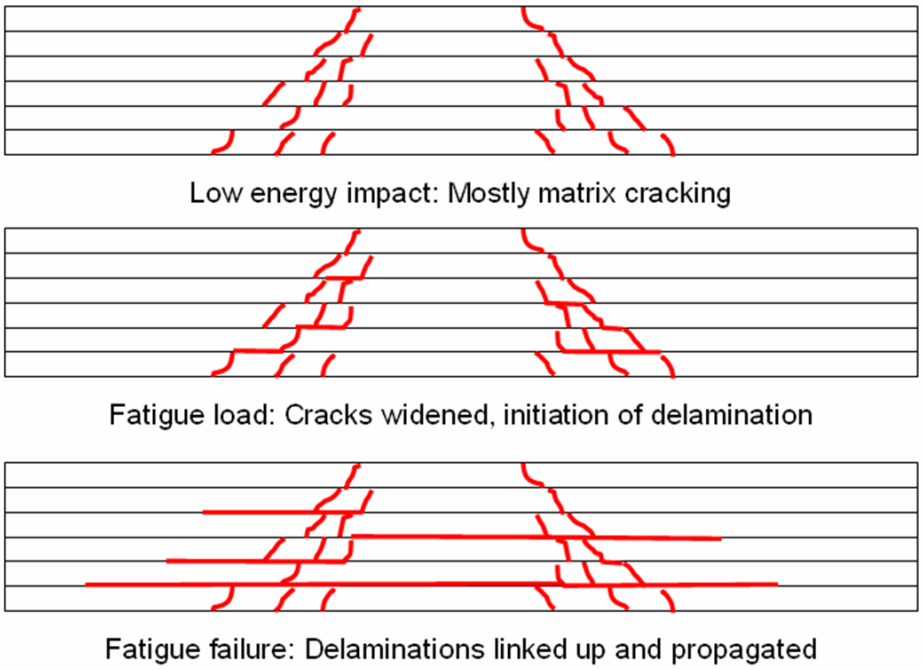

Figure 43. The Impact Damage and Fatigue Failure Process

4.2.3.6. Summary.

In the study of NDI for impact damage in solid laminates, impact-induced microcracks and delaminations in both carbon composites and glass composites were investigated, and both woven laminates and laminates of unidirectional plies were tested. The microscopic morphology of impact damage, especially in the energy range stradling the delamination threshold, was studied using optical microscopy on sectioned and polished samples. The well-known fact that damage severity increases with depth was verified by quantitative measurement of the distribution of microcrack density. The onset of delamination as the impact energy increased was found to be rather sudden, and the delamination size was steplike.

A fatigue test of samples containing low energy impact microcracks was conducted to observe the evolution of microcracks first into micro-delaminations and eventually into macro-delaminations and failure. The transition from short, localized micro-delaminations to extended macro-delaminations at the ply interfaces was slow in woven laminates and much faster in laminates of unidirectional prepreg plies. Ultrasonic detection of impact damage below and above the delamination threshold was studied. Regions containing micro-delaminations were not easily detected because they contributed only slightly to the attenuation of ultrasound (10% effect), but once macro-delaminations are formed, they effectively disrupted the ultrasonic propagation and were therefore easily mapped out with ultrasonic scans. Even though the tests conducted were on small, sectioned laboratory samples and the stress states in the fatigue test were not representative of what a composite structure would experience on an aircraft in the field, the general behavior of the progression from microcracks to delaminations can serve as a useful background and reference in future studies of composite damage and their NDE.

4.2.4 One-Sided Pitch-Catch Air-Coupled Ultrasound.

Some “cross pollenation” benefits between the FAA project and other CNDE projects are clear. The results can potentially lead to a new NDI approach for solid laminate structures. In our development of air-coupled ultrasonic methods in the past, through-transmission configuration that required access to both sides of the structure was primarily used. For H/C sandwich flight control components such as flaps and slats, two-sided access is often available. For load bearing primary structures of solid laminates, such as fuselage and wing skin, only one-sided access will be available. Recently, in an Army program for NDE of composite encapsulated ceramic tank armors, the ceramic tiles were imaged in thick armors (up to about 2 inches) using one-sided, pitch-catch air-coupled ultrasound. In subsequent work on NDE of wind turbine blades, pitch-catch ultrasound was used to detect and image “ply waviness” or wrinkles in thick glass fiber composites in wind turbines. In one-sided, pitch-catch inspection using air-coupled ultrasound, one must block out the specularly reflected signal that can easily overwhelm the weak Rayleigh wave or Lamb wave signals associated with the interior conditions of the structure. A simple solution has been found to eliminate the specular reflection signal by inserting the transmitting and receiving transducers into two slanted channels drilled in a block of closed-cell foam. The angles of the channels are drilled for optimal generation and reception of the wave mode used. By moving the foam block transducer holder over the surface of the structure, much like one would with a blackboard eraser, one-sided, pitch-catch inspection can be made with air-coupled ultrasound without the interference of the specular reflection. Using the foam block transducer holder, shown in figure 44, impact damage of solid composite laminates was detected. In

addition, the pitch-catch detection actually showed greater sensitivity than the normal incidence through-transmission air UT method for some flaws in wind turbine samples. It should also be noted that the one-sided air UT NDI was implemented on composites with simple, portable instrumentation that only consists of a UT flaw detector, preamplifier, and pair of high efficiency air-coupled transducers. For future development of one-sided pitch-catch air UT for aerospace composite structures, one should identify the wave modes that are most sensitive for detecting certain flaws and damage in the composite structure of interest, and drill the channels in the foam block at the corresponding angles to exploit the wave modes. The wave modes are expected to depend on the anisotropic elastic properties of the composite laminate, laminate thickness, and nature of the flaw and damage. The one-sided air UT approach was recently applied to composite structures and found the technique remarkably robust and adaptable. With its advantage of being non-contact and portable, the technique should be broadly exploited for the NDI of aircraft composite structures.

(a)

(b)

Figure 44. (a) One-Sided, Pitch-Catch Air UT Setup and Signal Produced by Impact Damage in GFRP Laminate and (b) Foam Block Transducer Holder Used on Wind Turbine Blade Trailing Edge

5. CONCLUSIONS.

An instrument was developed for this project to evaluate the ability of mechanical hysteresis measurements (or other measures of material nonlinear response) for characterizing impact damage in honeycomb (H/C) sandwich composite structures. It was demonstrated that although mechanical hysteresis (and an analog method referred to as sine-reference) are sensitive to impact-type defects in H/C composite sandwich structures, these methods, using the lightweight accelerometer as a tapping mass, do not offer enhanced sensitivity over standard tap test measurements of contact time, Tau, or stiffness, K. This is believed to be because of the low mass/velocity (kinetic energy) used, for which the response of the damaged material is not driven

beyond a linear (or nominally linear) response. Increased kinetic energy (mass or velocity) of the tap could increase the nonlinear response and, hence, sensitivity of the mechanical hysteresis measurements, but the potential for tap-related damage to the structure would certainly be higher.

In other work on solid laminate materials, the findings related to impact-induced microcracks, microcrack density, and the progression of microcracks to delaminations during fatigue is of particular interest. It was demonstrated that low-energy impacts, while creating local arrays of microcracks, are not trivial to detect with standard ultrasonic testing (UT) methods. Additional work with air-coupled UT demonstrated that significant utility is added by the use of one-sided pitch/catch (OSPC) techniques, when ply waviness (marcels), porosity, and resin-starved areas are detectable.

5.1 FUTURE DIRECTIONS.

Future work should involve continued investigations into the characterization of low-energy impacts where only microcracking is present. These impact-induced precursors to delamination damage are the earliest stage of damage likely to be detected by non-destructive methods, and the ability to detect and characterize these damage sites is essential. Microcrack density is a damage metric that could be introduced into fracture mechanics models, where these models could then predict the decrement to life or performance as a result of the impacts. The key is developing a nondestructive evaluation measurement metric that relates to the damage metric. UT methods, including angle beam longitudinal and shear modes as well as lamb and surface wave modes, should certainly be exploited. Specifically, air-coupled ultrasonic transmission (ACUT) methods for generating these modes should be used because of the very stable coupling conditions in ACUT. Measurements of the velocities of these various modes, if made over small volumetric regions, will relate to the local stiffness, which will be heavily influenced by microcracks. Attenuation and scattering parameters should also be examined with regard to microcrack arrays, which would initially involve the use of immersion and contact methods. Should these parameters be shown to be sensitive to microcrack density or other damage metrics, additional efforts should include ACUT, as the rock-steady coupling of ACUT would significantly simplify field/hanger measurements.

The utility of the OSPC arrangements in ACUT cannot be overemphasized. Where one-sided pitch catch ACUT really has shined is in its ability to generate and propagate plate and surface waves; in fact, the ability to propagate these waves around corners has been demonstrated, allowing inspection access to areas previously off limits to UT methods, such as the rear of the tubular spars in helicopter rotors. This ability to turn corners/mode convert at interfaces could also apply to bonded joints involving “L” and “T” section stiffeners. The most difficult part of inspecting nonplanar surfaces with UT methods is getting sound in when only a flat-surfaced contact probe is available. The ACUT excels with these applications and the one-side pitch/catch arrangement eliminates the need for two-sided access. The development of applications and methods; a thorough understanding of the range of modes available in this technique; and an understanding of how they can best be leveraged regarding inspection problems should continue.

6. REFERENCES.

1. Fiorino, F., "Rudder Alert," *Aviation Week and Space Technology*, April 3, 2006, p. 41

2. Pasztor, A., "Older Airbus Jets Get High-Tech Rudder Checks," *The Wall Street Journal*, December 19, 2007.

3. Hsu, K., "Nondestructive Testing Using Airborne Ultrasound," *Ultrasonics*, 44, Supp. 1, 2006, pp. 1019–1024.

4. Hsu, D. K., Peters, J.J., and Barnard, D.J., "Development of Fieldable Systems for Inspecting Aircraft Composite Structures," *Advances in Nondestructive Evaluation*, Trans Tech Publications, Switzerland, 2004, pp. 1845–1851.

5. Roach, D., and Rackow, K., "Improving In-Service Inspection of Composite Structures: It's a Game of Catt and Maus," *NASA/FAA/DOD Aging Aircraft Conference*, New Orleans, Louisiana, September 8–11, 2003.

6. Hsu, D.K., Barnard, D.J., and Peters, J.J., "Physical Basis of Tap Test as a Quantitative Imaging Tool for Composite Structures on Aircraft," *Review of Progress in Quantitative NDE*, Vol. 19, 2000, pp. 1857–1864.

7. Hsu, D.K., "Nondestructive Evaluation of Sandwich Structures," *Proceedings of the 8th International Conference on Sandwich Structures*, University of Porto, 2008, pp. 474–487.

8. Foreman, C., Dayal, V., Barnard, D.J., and Hsu, D.K., "Mechanical Hysteresis as NDE Tool for Evaluating Composite Honeycomb Damage," in *Review of Progress in Quantitative NDE, AIP Conf. Proc.* 1096, Melville, New York, 2009, pp. 1041–1048.

APPENDIX A—PUBLICATIONS AND PRESENTATIONS, BOOK CHAPTER, LIST OF FIELD TESTS/DEMONSTRATIONS, LIST OF COLLABORATORS, EXAMPLES OF SOFTWARE CODE

A.1 PUBLICATIONS AND PRESENTATIONS.

This project has led to 12 publications and a book chapter. They are listed below:

NDE 2009 – National Seminar and Exhibition on Non-Destructive Evaluation, December 2009 in Tiruchirappallai, India, "NDE of Heat Damage of Aerospace Composites Structures," David K. Hsu.

Pre-Conference Workshop, NDE 2009 – National Seminar and Exhibition on Non-Destructive Evaluation, December 2009 in Tiruchirappallai, India, "Air-Coupled Ultrasonic NDE: Principles and Applications," David K. Hsu.

Isampe Seminar (Keynote), December 2009, Bangalore, India, "NDE of Aerospace Composite Structures," David K. Hsu.

ASNT Annual Research Symposium and Spring Conference, March 2010, Williamsburg, VA, "Development of Instrumentation for Tap Test Based Mechanical Hysteresis Measurements and Imaging," D.J. Barnard, D.K. Hsu, T. Rohlfing, and A. Patz.

Review of Progress in Quantitative NDE, QNDE in San Diego, July 2010, "Development of a Portable Mechanical Hysteresis Measurement and Imaging System for Impact Characterization in Honeycomb Sandwich Structures," D.J. Barnard and D.K. Hsu, pp. 1743–1750.

SAMPE Conference in Seattle, WA, May 17–20, 2010, "NDE of Damage in Composites Based on Mechanical Stiffness and Hysteresis," D.K. Hsu and D.J. Barnard.

ASNT Conference on NDE of Aerospace Materials and Structures in St. Louis, MO, May 24–25, 2010, "NDE of Composites Using Terahertz Radiation," D.K. Hsu, C.P. Chiou, D.J. Barnard, K. H. Im, and J.W. Kim.

QNDE Conference, July 17–23, 2010 in San Diego, CA, "An Exploration of the Utilities of Terahertz Waves for the NDE of Composites," D.K. Hsu, K.H. Im, C.P. Chiou, and D.J. Barnard.

ASNT Research Symposium and Spring Conference, March 21–25, 2011 in San Francisco, Plenary Talk: "Innovations on the Cheap for Ultrasonic and Composite NDE," D.K. Hsu.

ASNT Research Symposium and Spring Conference, March 21–25, 2011 in San Francisco, "Microscopic Morphology, Failure Behavior, and NDT of Impact Damage in Solid Composite Laminates," D.K. Hsu, D.J. Barnard, Vinay Dayal, and Ajith Subramanian.

Airworthiness Assurance and Sustainment Conference, April 18–21, 2011 in San Diego, "Development of Tap Test Scanner for Quantitative NDE of Composite Sandwich Structures," D. J. Barnard and D. K. Hsu.

International Symposium on NDT of Materials and Structures (NDTMS), May 15–18, 2011 in Istanbul, Turkey, "A Study of Microcracks and Delaminations in Composite Laminates," D. K. Hsu, V. Dayal, M. Gerken, A. Subramanian, K. H. Im, and D. J. Barnard.

A.2 Book Chapter.

Chapter 17 "NDE for Aerospace Composites: Ultrasonic Inspection," in *Non-Destructive Testing: Evaluation and Application Within Polymer Matrix Composites*, Editor V. M. Karbhari, submitted by D. K. Hsu in December 2011, to be published by Woodhead Publishing Limited in UK.

A.3 LIST OF FIELD TESTS/DEMONSTRATIONS.

April 22, 2010 - Delta Air Lines, Minneapolis/St. Paul, MN, demo of early motorized tapper, CATT and ACUT coupled with portable flaw detector

Sept 22, 2010 – ATA NDT Forum demo at AANC/Sandia National Labs, Albuquerque, NM, demo of software and hardware operation of low speed A/D measurement circuit and motorized tapper.

A.4 LIST OF COLLABORATORS.

Jeff Nissen, Bell Helicopter – Thick skin honeycomb composite sandwich samples with defects.

Alex Melton, Delta Air Lines – Thin skin honeycomb composite sandwich samples – 2 Airbus A320 rudders.

Dennis Roach and Kirk Rackow, AANC Sandia – Thick solid laminate composite samples with engineered defects.

Steve Nolet, TPI Composites – Thick solid laminate samples with marcels and drypatch, naturally occurring and engineered.

A.5 EXAMPLES OF SOFTWARE CODE.

Motor Control Example:

```
OBJ 'For motor speed and direction control
  PC:"SerialMirror"
  BS2: "BS2_Functions"
VAR
  long PCin
  byte inc, speed, direction, new
  long Stack[100]
CON
  _clkmode= xtal1 + pll16x
  _xinfreq= 5_000_000
  BaudRate= 9600        'Baud
  RxPin= 31          'For RS232
  TxPin= 30          'For RS232
  'TxPin= 0          'sending to the motor controller
  CommsMode= %0000        'See SerialMirror.spin for meaning
PUB Start
  cognew(Motor, @Stack)
  Main
PUB Main
PC.start(RxPin, TxPin, CommsMode, BaudRate)
inc:=5
new:=0
direction:=0
  repeat
    PCin:=PC.rxcheck
    if PCin |= -1
      PCin := PC.rx
        if PCin == "1"
          inc := 1
        elseif PCin == "2"
          inc := 5
        elseif PCin == "3"
          inc := 10
        elseif PCin == "4"
          inc := 20
        elseif PCin == "f"
          speed := speed + inc
            if speed > 127
              speed := 127
        elseif PCin == "s"
          speed := speed - inc
            if speed < 0
              speed := 0
        elseif PCin == "x"
          speed := 0
        elseif PCin == "v"
          speed := 127
        elseif PCin == "w"
          direction := 0
        elseif PCin == "r"
          direction := 1
      new:=1
    PC.tx (60)            'outputs values to hyperterminal not used in
    PC.dec(direction)       'the VB program
```

```
  PC.tx (44)
  PC.dec(speed)
  PC.tx (44)
  PC.dec(inc)
  PC.tx (62)
  PC.rxflush
PUB Motor
 dira[0] := 1
 dira[1] := 1
 outa[0] := 1              'pin 0 = serial line
 outa[1] := 0              'pin 1 = reset line
 outa[1] := 1
 BS2.start (31,0)
 waitcnt(clkfreq / 10 + cnt)    'motor controller startup time
 speed := 0
 direction := 0
 BS2.Debug_Char(128)
 BS2.Debug_Char(0)
 BS2.Debug_Char(direction)
 BS2.Debug_Char(speed)
 repeat
  if new := 1
   BS2.Debug_Char(128)
   BS2.Debug_Char(0)
   BS2.Debug_Char(direction)
   BS2.Debug_Char(speed)
   new:=0
   waitcnt(120_000_000 + cnt)
  elseif new:=0
   BS2.Debug_Char(128)
   BS2.Debug_Char(0)
   BS2.Debug_Char(direction)
   BS2.Debug_Char(speed)
   waitcnt(120_000_000 + cnt)
```

A/D read and Average Example:

```
  CON
 _clkmode = xtal1 + pll4x
 _xinfreq = 5_000_000
 BaudRate= 115_200
 RxPin= 31
 TxPin= 30
 CommsMode= %0000                    'See SerialMirror.spin for meaning
OBJ
  debug : "PC_Debug"
 ' PC:    "SerialMirror"
  Full:   "FullDuplex"
VAR
 long time
 long PCin
 long Success
 long AvgStack[200]
 long MaxStack[100]
 long MinStack[100]
 long Answer1, Answer2, Answer3, Min1, MinDiv, Max1, MaxDiv
PUB Main
```

```
 waitcnt(100_000_000 + cnt)              'Wait 5 sec for prop to get ready
 time := 0
      waitcnt(clkfreq/100 + cnt)        'Calculates a future clock tick for cog syncronization
      time := (clkfreq/1 + cnt) #> 1
      cognew(AvgStart, @AvgStack)
      cognew(@jkl, @time)
      cognew(@AdcCog, @time)
PUB AvgStart
debug.start(115_200)
waitcnt(time)                           'Sync with other cogs
dira[1]:=1
waitcnt(44_796 + cnt)                   'Wait for first calc to be available Should be 63,389
repeat
 Answer1 := word[$7FFF]
 Answer3 := word[$7FF1]
 debug.dec(Answer1)
 debug.str(string("  "))
 debug.dec(Answer3)
 debug.crlf
DAT
         ORG      0
AdcCog       rdlong    temp1,par          'Wait for value to be non-zero
         tjz      temp1,#AdcCog
         waitcnt   temp1,#0           'Wait for synchronization point
         mov      dira, DIRA_DEFN      'Define Inputs and Outputs
         nop                          'Keep timing even with other cogs
         nop
:BigLoop
         mov      AdcValue, ADC_DEFN   'Clears the Value of AdcValue
         mov      outa, CsAdc         'Chip Select High
         andn     outa, CsAdc         'Chip Select Low
         mov      outa, Outa_1         'ControlByte
         mov      outa, Outa_2
         mov      outa, Outa_4
         mov      outa, Outa_5
         mov      outa, Outa_1
         mov      outa, Outa_2
         mov      outa, Outa_1
         mov      outa, Outa_2
         mov      outa, Outa_4
         mov      outa, Outa_5
         mov      outa, Outa_4
         mov      outa, Outa_5
         mov      outa, Outa_4
         mov      outa, Outa_5
         mov      outa, Outa_1
         mov      outa, Outa_2
                          '************ End of Control Byte
         mov      outa, Outa_4        'Extra Clock Cycles for Aquisition
         mov      outa, Outa_5
         mov      outa, Outa_4
         mov      outa, Outa_5
         mov      outa, Outa_4
         mov      outa, Outa_5
```

```
mov     outa, Outa_4
                    '************ End of Aquisition
mov     outa, Outa_5
mov     outa, Outa_4

nop                 '************ Strobe Goes Low Here
mov     outa, Outa_5        'Shift In Starts Here
mov     outa, Outa_4
nop
nop
and     AoutAdc, ina    wc, nr
rcl     AdcValue, #1
mov     outa, Outa_5            'Clock High
mov     outa, Outa_4            'Clock Low
nop                         'Wait for ADC to Output New Bit
nop
and     AoutAdc, ina    wc, nr    'Read Bit  nr=not write to var AoutAdc
rcl     AdcValue, #1            'Rotates Left 1 Bit to Form a Wor
mov     outa, Outa_5
mov     outa, Outa_4
nop
nop
and     AoutAdc, ina    wc, nr
rcl     AdcValue, #1
mov     outa, Outa_5
mov     outa, Outa_4
nop
nop
and     AoutAdc, ina    wc, nr
rcl     AdcValue, #1
mov     outa, Outa_5
mov     outa, Outa_4
nop
nop
and     AoutAdc, ina    wc, nr
rcl     AdcValue, #1
mov     outa, Outa_5
mov     outa, Outa_4
nop
nop
and     AoutAdc, ina    wc, nr
rcl     AdcValue, #1
mov     outa, Outa_5
mov     outa, Outa_4
nop
nop
and     AoutAdc, ina    wc, nr
rcl     AdcValue, #1

mov     outa, Outa_5
mov     outa, Outa_4
nop
nop
and     AoutAdc, ina    wc, nr
```

```
        rcl     AdcValue, #1
        mov     outa, Outa_5
        mov     outa, Outa_4
        nop
        nop
        and     AoutAdc, ina    wc, nr
        rcl     AdcValue, #1
        mov     outa, Outa_5
        mov     outa, Outa_4
        nop
        nop
        and     AoutAdc, ina    wc, nr
        rcl     AdcValue, #1
        mov     outa, Outa_5
        mov     outa, Outa_4
        nop
        nop
        and     AoutAdc, ina    wc, nr
        rcl     AdcValue, #1
        mov     outa, Outa_5
        mov     outa, Outa_4
        nop
        nop
        and     AoutAdc, ina    wc, nr
        rcl     AdcValue, #1
        mov     outa, Outa_Cs           'Chip Select High to Terminate Cycle
        wrword  AdcValue, ToStuff       'Writes the Word(16 Bits) from the Shift In
        jmp     #:BigLoop               'Jump to Top
Outa_1      long    %0000_0000_0000_0000_0000_0000_0000_0001
Outa_2      long    %0000_0000_0000_0000_0000_0000_0100_0001
Outa_4      long    %0000_0000_0000_0000_0000_0000_0000_0000
Outa_5      long    %0000_0000_0000_0000_0000_0000_0100_0000
Outa_Cs     long    %0000_0000_0000_0000_0000_0000_0001_0000
DIRA_DEFN   long    %0000_0000_0000_0000_0000_0000_1101_0001
ADC_DEFN    word    %0000_0000_0000_0000
CsAdc       long    %0000_0000_0000_0000_0000_0000_0001_0000
AoutAdc     long    %0000_0000_0000_0000_0000_0000_0000_0100
Watch       long    %0000_0000_0000_0000_0000_0000_1000_0000
ToStuff     long    $7FFF
AdcValue    long    0
temp1               res 1
DAT
        ORG     0               'This cog adds and divdes the values sent from ADCcog
                                'There are four sets on 25 addition and division processes
                                'These 4 are added and the cog outputs the average of 100 values
jkl
        rdlong  temp3,par       '*Wait for value to be non-zero
        tjz     temp3,#jkl      '*Syncs all cogs together
        waitcnt temp3,#0        '*
        mov     pause, cnt      'Initial wait for one full A/D cycle
        add     pause, #443
        waitcnt pause, #0
        mov     dira, pin7      'Pin7 is now an output
        mov     counts, #25     'Setting initial values for these variables
```

```
        mov     final, #0
        mov     div, #0
        mov     y, #0
:loop0
        mov     outa, pin7          'Spike to be seen on scope
        nop
        nop
        xor     outa, pin7
        rdword  cc, frmad           'Reads value from ADC cog
        mov     div, cc             'Moves this value into another variable
        mov     y,#25               'divide by 25  'get divisor into y[30..15]
        shl     y,#15
        mov     count,#16           'ready for 16 quotient bit
:loop0_0    cmpsub  div,y  wc       'if y =< x then subtract it, quotient bit into c
        rcl     div,#1              'rotate c into quotient, shift dividend
        djnz    count,#:loop0_0     'loop until done
        add     final, div          'Adds the divided number to a variable containing the total of all 25 values
        mov     count01, cnt        'Waitcnt for syncronization with ADC cog
        add     count01, #181       'should be #185
        waitcnt count01, #0
        djnz    counts, #:loop0     'Decrement Jump if Not Zero: Loops only 25 times
:loop
        mov     outa, pin7
        nop
        nop
        xor     outa, pin7
        wrword  final, word1        'Writes the first 25 averaged values to memory
        mov     counts, #25         'Resets variables for next cycle
        mov     div, #0
        mov     final, #0
        mov     count011, cnt       'Waitcnt to syncronize with the add and divide cycles
        add     count011, #386
        waitcnt count011, #0
        nop
:loop1
        mov     outa, pin7
        nop
        nop
        xor     outa, pin7
        rdword  cc, frmad
        mov     div, cc
        mov     y,#25               'divide by 500 (~100 sps) 'get divisor into y[30..15]
        shl     y,#15
        mov     count,#16           'ready for 16 quotient bit
:loop1_1    cmpsub  div,y  wc       'if y =< x then subtract it, quotient bit into c
        rcl     div,#1              'rotate c into quotient, shift dividend
        djnz    count,#:loop1_1     'loop until done
        add     final, div
        mov     count01, cnt
        add     count01, #181
        waitcnt count01, #0
        djnz    counts, #:loop1
        mov     outa, pin7
        nop
```

```
        nop
        xor     outa, pin7
        wrword  final, word2
        mov     counts, #25
        mov     div, #0
        mov     final, #0
        mov     count011, cnt
        add     count011, #386
        waitcnt count011, #0
        nop
:loop2
        mov     outa, pin7
        nop
        nop
        xor     outa, pin7
        rdword  cc, frmad
        mov     div, cc
        mov     y,#25           'divide by 500 (~100 sps) 'get divisor into y[30..15]
        shl     y,#15
        mov     count,#16       'ready for 16 quotient bit
:loop2_2    cmpsub  div,y   wc      'if y =< x then subtract it, quotient bit into c
        rcl     div,#1          'rotate c into quotient, shift dividend
        djnz    count,#:loop2_2     'loop until done
        add     final, div
        mov     count01, cnt
        add     count01, #181
        waitcnt count01, #0
        djnz    counts, #:loop2
        mov     outa, pin7
        nop
        nop
        xor     outa, pin7
        wrword  final, word3
        mov     counts, #25
        mov     div, #0
        mov     final, #0
        mov     count011, cnt
        add     count011, #386
        waitcnt count011, #0
        nop
:loop3
        mov     outa, pin7
        nop
        nop
        xor     outa, pin7
        rdword  cc, frmad
        mov     div, cc
        mov     y,#25           'divide by 25 'get divisor into y[30..15]
        shl     y,#15
        mov     count,#16       'ready for 16 quotient bit
:loop3_3    cmpsub  div,y   wc      'if y =< x then subtract it, quotient bit into c
        rcl     div,#1          'rotate c into quotient, shift dividend
        djnz    count,#:loop3_3     'loop until done
        add     final, div
```

```
        mov     count01, cnt
        add     count01, #181       'should be #185
        waitcnt  count01, #0
        djnz    counts, #:loop3
        mov     outa, pin7
        nop
        nop
        xor     outa, pin7
        wrword  final, word4
        mov     counts, #25
        mov     div, #0
        mov     final, #0
        mov     count011, cnt
        add     count011, #386      'should be #185
        waitcnt  count011, #0
        'jmp    #:loop0
'*****************************************************************************************************
                                'This section as the 4 groups of 25 values
        mov     outa, pin7
        nop
        nop
        xor     outa, pin7
        rdword  word01, word1       'Reads the 4 words and adds then all together
        add     total, word01
        rdword  word02, word2
        add     total, word02
        rdword  word03, word3
        add     total, word03
        rdword  word04, word4
        add     total, word04
        mov     y, #4               'Divides the 100 values
        shl     y, #15
        mov     count, #16
:loop4_4    cmpsub  div,y  wc       'if y =< x then subtract it, quotient bit into c
        rcl     div,#1              'rotate c into quotient, shift dividend
        djnz    count,#:loop4_4
        wrword  div, wordfinal      'This is the final average of 100 values
        mov     total, #0           'Resets theses values for next cycle
        mov     final, #0
        mov     count01, cnt        'Waitcnt for syncronization
        add     count01, #83
        waitcnt  count01, #0
        jmp     #:loop0
pause       long    0
pin7        long    |<3
div         long    0
y           long    0
counts      long    0
count01     long    0
count011    long    0
count       long    0
word01      long    0
word02      long    0
word03      long    0
```

```
word04      long    0
word1       long    $7FF0
word2       long    $7FEE
word3       long    $7FEC
word4       long    $7FEA
frmad       long    $7FFF
wordfinal   long    $7FF1
final               res 1
temp3               res 1
cc                  res 1
total               res 1
```